1   **Revision 2**

2

3   # High-pressure phase transitions of $Fe_{3-x}Ti_xO_4$ solid solution

4   # up to 60 GPa correlated with electronic spin transition

5

6   Takamitsu Yamanaka[1], Atsushi Kyono[1,2], Yuki Nakamoto[1,3], Yue Meng[4], Svetlana Kharlamova[5], Victor V.

7   Struzhkin[1] and Ho-kwang Mao[1,2,3]

8

9   [1] *Geophysical Laboratory, Carnegie Institution of Washington. Washington, D.C. 20015*

10   [2] *Division of Earth Evolution Sciences, Graduate School of Life and Environment Sciences, University of*

11   *Tsukuba, Tsukuba Japan*

12   [3] *Center of Quantum Science and Technology under Extreme Conditions Osaka University, Osaka, Japan*

13   [4] *High Pressure Collaborative Access Team, Geophysical Laboratory, Carnegie Institution of Washington,*

14   *Argonne, Illinois, 60439, USA*

15   [5] *High Pressure Synergetic Consortium, Geophysical Laboratory, Carnegie Institution of Washington,*

16   *Argonne, Illinois, 60439, USA*

17

18   *tyamanaka@ciw.edu*

19

20

21   Abstract

22   Structure transition of the titanomagnetite ($Fe_{3-x}Ti_xO_4$) solid solution under pressures up to 60 GPa has been

23   clarified by single crystal and powder diffraction studies using synchrotron radiation with diamond anvil

24   cell. Present Rietveld structure refinements of the solid solution prove that the most preferable cation

25   distribution is based on the crystal field preference rather than the magnetic spin ordering in the solid

26   solution.

27   The Ti-rich phases in $0.734 \leq x \leq 1.0$ undergo transformation from the cubic spinel of $Fd\overline{3}m$ to the tetragonal

28   spinel structure of $I4_1/amd$ with c/a<1.0 by Jahn-Teller effect of $^{IV}Fe^{2+}$ ($3d^6$) in the tetrahedral site. The

29   c/a<1 ratio is induced by the resolution of degeneracy of e orbital and $d_{x^2-y^2}$ orbital is placed in the lower

30   electronic state than d_{z^2}. The distortion identified by c/a<1 is more intensively observed with increasing Ti

31   content in the $Fe_{3-x}Ti_xO_4$ solid solutions and with increasing pressure. X-ray emission experiment of

1

32 Fe_2TiO_4 at high pressures confirms the spin transition of Fe-$K\beta$ from high spin to intermediate spin (IS)

33 state. High spin (HS)-to-low spin (LS) transition starts from 14 GPa and IS state gradually increases with

34 compression. $^{VI}Fe^{2+}$ in the octahedral site is more capable for the HS-to-LS transition, compared with Fe^{2+}

35 in the four-fold or eight-fold coordinated site.

36 The transition to orthorhombic post-spinel structure of *Cmcm* has been confirmed in the whole

37 compositional range of $Fe_{3-x}Ti_xO_4$. The transition pressure decreases from 25 GPa (x=0.0) to 15 GPa

38 (x=1.0) with increasing Ti content. There are two cation sites in the orthorhombic phase: M1 and M2 sites

39 of eight-fold and six-fold coordination sites. Fe^{2+} and Ti^{4+} are disordered in the M2 site. This structure

40 change is accelerated at higher pressures due to spin transition of Fe^{2+} in the octahedral site. This is because

41 the ionic radius of $^{VI}Fe^{2+}$ becomes 20% shortened by the spin transition. At 53 GPa, the structure transforms

42 to another high-pressure polymorph of *Pmma* with the ordered structure of Ti and Fe atoms in the

43 octahedral site. This structure change results from the order-disorder transition.

44

45 Introduction

46 High-pressure phase transitions of many spinel compounds in the earth crust have attracted much

47 attention from geophysical interests. Many spinels decompose directly or indirectly to ilmenite+B1,

48 rutile+B1, and perovskite+B1 with increasing pressure. However, some spinels transform to the

49 high-pressure post-spinel phases without decomposition. High-pressure studies of spinels also attract

50 extensive attention in order to understand strong electronic correlation such as charge transfer, electron

51 hopping, electron high-low spin transition, Jahn-Teller distortion, and charge disproportion in the lower

52 mantle or subduction zone.

53 Solid solution of titanomagnetite ($Fe_{3-x}Ti_xO_4$) between magnetite (Fe_3O_4) and ulvöspinel (Fe_2TiO_4) is

54 one of the principal magnetic substances used for the investigation of rock magnetism. The magnetic

55 property changes from ferrimagnetic magnetite Fe_3O_4, to antiferromagnetic ulvöspinel Fe_2TiO_4 with

56 increasing Ti content. A number of studies of the cation distribution in the solid solution have been carried

57 out and the distribution has been examined (Akimoto, 1954; Neel, 1955; Chevallier et al, 1955; O'Reilly

58 and Banerjee, 1965; Lindsley, 1976; Kakol et al., 1992; Pearce et al, 2006). These models were proposed

59 from the diffraction studies using X-ray and neutron sources, magnetic susceptibility measurements and

60 X-ray absorption. They are described by cation site preference based on crystal field, relative cation size

61 and magnetic moment. Wechsler et al., (1984) reported almost the same result of the Akimoto model from

62 their X-ray-neutron studies. Bosi et al. (2009) discussed the crystal chemistry of the $Fe_{3-x}Ti_xO_4$ solid

63 solutions as a function of Ti composition by X-ray single-crystal diffraction study.

2

64   Several experiments have been devoted to magnetite under high-pressure (HP) conditions by X-ray

65   powder diffraction (Mao et al. 1974; Pasternak et al. 1994; Fei et al. 1999; Haavik et al. 2000; Kuriki et al.

66   2002; Dubrobinsky et al., 2003; Rozenberg et al. 2007) and single-crystal X-ray diffraction (Finger et al.

67   1986; Nakagiri et al. 1986; Reichmann and Jacobsen 2004). Magnetite undergoes a phase transition to a HP

68   form, called h-Fe_3O_4, above 25 GPa. Haavik et al. (2000) investigated the elastic behavior, the stability field

69   and the crystal structure of the HP form of magnetite, showing that h-Fe_3O_4 has the $CaTi_2O_4$-type structure

70   with space group *Bbmm* (*Cmcm*). Metallization of magnetite under high-pressure was reported by electrical

71   resistivity measurements by Todo et al. (2001) and they reported that the Verwey transition temperature

72   decreases non-linearly with increasing pressure and the transition disappears at around 7.5 GPa. The similar

73   spinel solid solution of $Fe_{3-x}Si_xO_4$ as titanomagnetite has been investigated to explain the electron

74   conductivity and magnetic anisotropy in the crust (Yamanaka et al., 2001a, 2001b).

75   A systematic study of the Raman spectra of titanomagnetite for x=0.0, 0.2, 0.4 and 0.6 has been

76   conducted (Zinii et al., 2011). Raman spectroscopic study of ulvöspinel has been undertaken in a

77   diamond-anvil cell under hydrostatic conditions up to 57 GPa at room temperature (Kyono et al., 2011).

78   The Jahn-Teller effect on the structure transition of $Fe_{3-x}Ti_xO_4$ has been investigated at high pressures and

79   low temperatures (Yamanaka et al., 2009). The phase transition takes place at 8 GPa with increasing

80   pressure at ambient temperature and the transition was also found at −110 °C and ambient pressure. The

81   former has $c/a = 0.9982$••at 11.43 GPa and the latter c/a = 1.0035 at −170 °C. These indicate that the

82   degeneracy of e orbit of Fe^{2+} at the tetrahedral site is in a different resolved manner under high-pressure and

83   low-temperature conditions: the former prefers electronic state $d_{x^2-y^2}$ and the latter d_{z^2} orbit in e orbit due to

84   Jahn-Teller effect of Fe^{2+} at the tetrahedral site.

85   The present experiment aims to elucidate the structure transition of Fe_2TiO_4 and electronic spin transition

86   of Fe using an X-ray emission study of Fe$K\beta$ under high pressure. Elucidating the correlation between

87   structure and spin state is one of the crucial problems for understanding the geophysical properties of earth

88   interiors under high pressure such as electric conductivity, magnetic properties and elastic properties.

89

90   Experiment

91   Powder samples of $Fe_{3-x}Ti_xO_4$ solid solutions were prepared by solid-solid reaction at ambient pressure.

92   In order to prepare the stoichiometric samples, special care was taken into for controlling partial pressure of

93   oxygen (Po_2) using CO and CO_2 gas mixture. The well-defined single-crystal sample of Fe_2TiO_4 ulvöspinel

94   (x=1.0) was synthesized using the floating zone method and it was used for the high-pressure diffraction

3

95   study. The chemical compositions of all synthesized samples were analyzed by electron probe

96   microanalyzer (EPMA) and the homogeneity was examined by the back-scattered electron images. Neither

97   trace element nor impurity was found in the samples.

98   X-ray powder diffraction experiments were executed using a diamond anvil cell (DAC) at pressures up

99   to 61 GPa at ambient temperature. Rhenium gasket was preindented from 200 μm to 50 μm. Pressure was

100 measured 20 min after changing the pressure to ensure that the sample was held at stable pressure. Pressure

101 was determined by the ruby fluorescence method (Piermarini et al., 1975; Mao et al., 1986). The powder

102 sample and ruby-chip pressure marker were placed in the gasket hole of 125 μm in diameter. Neon pressure

103 transmitting medium was used in all present experiments. Angular-dispersive powder diffraction

104 measurements of $Fe_{3-x}Ti_xO_4$ solid solution (x=0.0, 0.102, 0.231, 0.551, 0.624, 0.734, 0.831, 1.0) were

105 undertaken at the undulator beam line BL-13A with wavelength about 30 KeV and at the bending magnet

106 beam line BL-18C with 20 KeV in Photon Factory (KEK), Tsukuba. A powder diffraction study of Fe_2TiO_4

107 under pressure up to 61GPa was also conducted by angular-dispersive powder XRD experiment with

108 wavelength 0.4218 Å at 16-BM-D at the Advanced Photon Source (APS), Argonne National Laboratory.

109 The long camera length system at KEK was applied for the precise measurement of the lattice constant.

110 The high-resolution diffraction profile analysis was performed within $2\theta=5°\sim15°$ using a narrow collimator

111 of 10 μm.

112   Fe-$K\beta$ X-ray emission spectroscopy (XES) of Fe_2TiO_4 has been undertaken at 16-ID-B in APS in order

113 to clarify the spin state change under pressure up to 30.9 GPa. The measurement of the $K\beta$ fluorescence

114 reveals changes in the $3d$ electronic configuration of the Fe in the sample. XES measurement has

115 confirmed the high-low spin transition. The incident X-ray beam was focused using a pair of

116 Kirkpatrick-Baez mirrors. A spherically bent Si (333) crystal was used for the energy analyzer, which is

117 placed along with the detector with a high resolution of 0.5 eV. The incident X-ray beam first passes

118 through a diamond monochromator, which selects X-ray energy around the Fe-$K\beta$ absorption edge. The

119 Fe-$K\beta$ emission spectrum is detected through the gasket. The analyzer angle θ and detector angle 2θ

120 simultaneously scan for changing energy along the Rowland-circle in the spectrometer scans. Helium gas

121 was filled in the X-ray path in order to reduce an absorption by air. The detailed specification was reported

122 in Rueff et al., (1999).

123

124 Structure change with composition and pressure of $Fe_{3-x}Ti_xO_4$ solid solutions

4

125   The structural analyses of the pressurized samples were undertaken by the Rietveld profile fitting

126   method. The Rietveld refinement was conducted using the program RIETAN-2000 (Izumi and Ikeda,

127   2000). First the background intensity distribution was adjusted for the refinement. Then lattice constants,

128   atomic positional coordinates and temperature factors were treated as variable parameters and subsequently

129   profile parameters and site-occupancy parameters were varied in the refinement. Finally a full matrix

130   least-squares refinement was conducted. The full-width half-maximum parameter, asymmetry parameters

131   and peak profile function confirm that the diffraction data can guarantee a reliable profile analysis.

132   Rietveld fitting indicates the continuous increase of the lattice constant as a function of composition x in

133     $Fe_{3-x}Ti_xO_4$ at ambient conditions (Table 1). The site occupancy refinements are performed in consideration

134   of chemical constraint based on the EPMA analysis. Since the atomic numbers of Fe and Ti are 26 and 22,

135   they are noticeably different enough to identify atoms in X-ray scattering power. The cation distribution of

136     $Fe^{2+}(24)$ and $Fe^{3+}(23)$ cannot be determined by X-ray diffraction because of their similar atomic scattering

137   factors.

138   In the present single crystal diffraction experiment, effective charge analysis has not been undertaken

139   with monopole κ-parameter refinement using the data set of the diffraction intensities. The site occupancy

140   refinement indicates Ti ion preferentially occupies the octahedral site in the whole compositional range.

141   This is in accordance with the neutron diffraction study of Forster and Hall (1965).

142   The oxygen positional parameter, (u u u), continuously changes with the content of Fe_2TiO_4

143   component. A-O and B-O bond distances in $^{IV}A^{VI}B_2O_4$ spinel structure reflect the cation distribution. The

144   AO_4 tetrahedral volume shows a noticeable increase, because of the large difference in ionic radii between

145   Fe^{2+} (0.63Å) and Fe^{3+} (0.49Å) (Shannon et al., 1976) . On the other hand the volume of the BO_6 octahedron

146   decreases slightly by the replacement of Ti^{4+} (0.605Å) for Fe^{3+} (0.63Å). With increasing substitution of Ti^{4+}

147   for Fe^{3+} in the octahedral site, simultaneous substitution of Fe^{2+} for Fe^{3+} takes place in the tetrahedral site.

148   The compositional dependence of the bond distances and site volumes is shown in Figure 1.

149   Magnetite transforms to the orthorhombic phase (h-Fe_3O_4) at 25 GPa. The diffraction peaks of the

150   spinel phase were detected at pressures even at 50 GPa. With decreasing pressure the back transformation

151   to the spinel phase could not be confirmed, because the spinel peaks remained in the entire pressure range.

152   A large hysteresis of the structural transition was observed in the compositional range of 0.0<x<0.551.

153   Samples with a large amount of iron content show a more obvious hysteresis. The two-phase mixture of

154   magnetite and h-Fe_3O_4 were reported above the transition pressure (Mao et al., 1974; Huang and Bassett

155   1986; Pasternak et al., 1994). The spinel phase of $Fe_{3-x}Ti_xO_4$ in the compositional range was found in the

156   orthorhombic region in the present experiment.

5

157   At ambient temperature, the cubic spinel structure of Fe_2TiO_4 with space group $Fd\bar{3}m$ $Z=8$ transforms

158   to tetragonal spinel structure of $I4_1/amd$ $Z=4$ at about 8 GPa, and it is confirmed that the transition is

159   reversible. Subsequent transition from the tetragonal to the orthorhombic post-spinel phase is observed at

160   about 15 GPa.

161   The phase stability of the $Fe_{3-x}Ti_xO_4$ solid solutions was presented in our previous paper (Figure 1 in

162   Yamanaka et al., 2009) as functions of pressure and composition at ambient temperature. The transition

163   pressure from cubic spinel to an orthorhombic post-spinel phase decreases from 25 GPa at x=0.0 to 15 GPa

164   at x=1.0 with an increase in the Ti content. The tetragonal phase appears only in the compositional region of

165   x>0.734. The transition pressure decreases with Ti substitution. The back transformation from the

166   post-spinel phase to the tetragonal spinel could not be confirmed with decreasing pressure. And under

167   further decreasing pressure the post-spinel phase directly transforms to the spinel phase without showing a

168   tetragonal phase. Consequently the post-spinel phase of Fe_2TiO_4 is unquenchable.

169   Lattice constants of the spinel solid solutions $Fe_{3-x}Ti_xO_4$ are presented as a function of pressure in

170   Table 1. All spinel structures of $Fe_{3-x}Ti_xO_4$ yield almost monotonous compression curves before the

171   transition to high-pressure phases, as shown in Figure 2.

172

173   Bulk modulus of the $Fe_{3-x}Ti_xO_4$ spinel solid solutions

174   The bulk modulus of the spinel phase is calculated by the second-order Birch-Murnaghan (BM)

175   equation of state from the unit cell volumes. These data of K_0' are larger than $K_0'=4$. The bulk modulus of

176   Fe_3O_4 (x=0.0) is $K_0=183.4(8.1)$ GPa and $K_0'=7.1(2.9)$ in good agreement with the previously reported data:

177   181(2) GPa (Nakagiri et al., 1985): 217(2) GPa (Haavik et al., 2000) and 180.6(1.1) GPa (Rozenberg et al.,

178   2007). Since the spinels with large content of Ti (x>0.624) have a small pressure range of the cubic phase,

179   the number of observed data is limited to only five data. Then those data applying the first-order BM are

180   more reliable. The bulk modulus presented shown in Table 2 increases with Ti content. It is clarified that

181   Fe_2TiO_4 ulvöspinel has a much larger K_0 than magnetite.

182

183   Tetragonal phase induced by Jahn-Teller effect

184   The reflections observed by the high-resolution powder diffraction system in KEK were identified as

185   the tetragonal structure with $c/a<1$. The c/a ratios are 0.9846 of x=0.831 at 12.45 GPa and 0.9787 of x=1.0

186   at 11.43 GPa. The samples with x=0.734, 0.831 and 1.0 transform to the tetragonal phase at about 12 GPa,

187   9 GPa, and 8 GPa, respectively. The unit cell volume changes at the transition pressures from the cubic to

188   tetragonal phase indicate that the transformation is a first-order transition. Tetragonal spinel structure of

6

189   $I4_1/amd$ was induced from the tetragonal distortion due to the Jahn-Teller (J-T) effect of Fe^{2+} ($3d^6$) at the

190   tetrahedral site (Yamanaka et al., 2009), although the J-T tetragonal distortion due to Fe^{2+} in the tetrahedral

191   site is a very rare case among many substances. The tetrahedral site symmetry changes from $\bar{4}3m$ to $\bar{4}2m$.

192   The tetragonal phase is not found in the samples with x<0.624. Probably those samples may have a

193   tetragonal distortion, but it cannot be observed because the distortion is too small to be detected by

194   diffraction study. The tetragonal distortion is enhanced with increasing pressure, as shown in Figure 3. The

195   enhancement can be energetically interrelated to the enlargement of the splitting energy Dq between t and e

196   orbitals with pressure.

197

198   Orthorhombic high-pressure phases of Fe_2TiO_4

199   Much attention has been paid to the post-spinel structures because of their geophysical interests Three

200   orthorhombic phases of $CaMn_2O_4$ (*Pmab* Z=4) (Andrault and Casanova, 2001; Waskowska et al., 2001),

201   $CaTi_2O_4$ (*Cmcm,* Z=4)   (Funamori et al., 1998; Haavik et al., 2000; Dubrobinsky et al, 2003) and $CaFe_2O_4$

202   (*Pnam,* Z=4) (Reid and Ringwood, 1969; Irifune et al., 1991; Akaogi et al., 1999) have been reported as

203   high-pressure polymorphs of spinels. The single-crystal structure analyses were reported: $CaMn_2O_4$ by

204   Geisber et al., (2001), $CaTi_2O_4$ by Rogge (1998) and $CaFe_2O_4$ by Becker and Kasper (1957). Ca has an

205   eight-fold coordination in three structures and Mn, Ti, and Fe occupy the six-fold coordination sites. In

206   these three structures, two polyhedra are linked with the shared edges and shared corners. Hence these

207   structures are much denser than the spinel structure. All three samples have further high-pressure

208   polymorphs (Yamanaka et al., 2008). $CaMn_2O_4$ transforms to the $CaTi_2O_4$-type structure. A new phase of

209   $CaFe_2O_4$ has a space group *Pnam* due to martensitic transformation by displacing atoms in every third layer

210   perpendicular to the c axis. $CaTi_2O_4$ also has a new high-pressure polymorph with space group *Cmcm*

211   (*Bbmm*).

212   Mao et al., (1974) first described high-pressure magnetite at pressure over 25GPa, Fei et al (1999)

213   reported Fe_3O_4 transformation to $CaMn_2O_4$ (h- Fe_3O_4) at 24 GPa at 823 K. However, Haavik et al. (2000)

214   described the transition to $CaTi_2O_4$ at 21.8 GPa at ambient temperature and Reichmann and Jacobsen

215   (2004) reported that pressure-induced shear-mode softening in magnetite is related to magnetoelastic

216   coupling and the orthorhombic structure is stable above 21GPa. There are some discrepancies in post-spinel

217   structures, because of their structural similarity.

218   In the present experiment of $Fe_{3-x}Ti_xO_4$, the transition pressure to the $CaTi_2O_4$-type structure of *Cmcm*

219   decreases from 25 GPa (x=0.0) to 15 GPa (x=1.0) with increasing Ti content in the solid solution. The

220   *Cmcm* structure of Fe_2TiO_4 is stable up to 50 GPa. The pressurized sample at 27 GPa was kept in a DAC

221   for 5 days at 200 $^{\circ}$C in order to avoid the mixture of the spinel phase. Rietveld profile fitting to the

222   diffraction pattern taken at 40 GPa confirms the $CaTi_2O_4$ type structure, as shown in Figure 4. The structure

223   obtained by the Rietveld analysis is shown in Figure 5. The results of the Rietveld analyses at selected

224   pressures are listed in Table 3. The bond distances of polymorphs, cubic, tetragonal and two orthorhombic

225   phases of Fe_2TiO_4 are presented in Table 4. There are two cation sites in the orthorhombic phase with the

226   space group *Cmcm*; M1 (4c) and M2 (8f) atoms are located in the eight-fold and six-fold coordination sites,

227   respectively. One of the Fe^{2+} occupies the M1 site and the other is disordered in the M2 site with Ti^{4+}, as

228   shown in Figure 5. M2 octahedra are linked to make a herringbone-shape structure. The present profile

229   fitting analyses at pressures up to 50 GPa cannot detect the cation ordering of   Fe and Ti in the M2 site.

230   The orthorhombic $CaTi_2O_4$-type structure is found in the whole compositional range of $Fe_{3-x}Ti_xO_4$ solid

231   solutions. In the h-Fe_3O_4 structure, Fe^{2+} occupies the 8-fold coordinated M1 site and two Fe^{3+} are located in

232   the octahedral M2 site. On the other hand, the high-pressure form of Fe_2TiO_4 has Fe^{2+} in M1 and Ti^{4+} and

233   Fe^{2+} in the M2 site, which is determined by site occupancy analysis. The octahedral bonds in the

234   orthorhombic structure are noticeably compressed with increasing pressure (Table 4). The extremely

235   shortened octahedral bonds cause a distortion of the eight-fold cation site, which has shared edges with the

236   octahedral site.

237   At pressures above 53 GPa the structure refinement based on *Cmcm* does not produce reasonable

238   bond lengths resulting in a very poor reliable factors. In the *Cmcm* structure, the Fe^{2+} ion in the M2

239   octahedral site is in the low-spin state, and it has an extremely small ion radius. Two octahedral sites

240   provide an ordered cation distribution. *Pmma* (*Pmcm*) is a possible candidate for two octahedral sites,

241   which is a non-isomorphic subgroup of *Cmcm*, and loses the *C*-centered symmetry. The M1 and M2 sites

242   of the *Cmcm* structure are both split into two crystallographic nonequivalent sites in *Pmma*. Fe atoms are

243   located in two eight-fold coordination sites, 2e and 2f, and Fe and Ti are separately situated in the six-fold

244   coordination sites, 4i and 4j, respectively. Rietveld profile fitting including a variable parameter of the site

245   occupancy of the *Pmma* structure at 61 GPa converged with a much higher reliability factor than that of the

246   *Cmcm* structure (Figure 6). The converged structure obtained from the Rietveld refinement is presented in

247   Figure 7. The calculated patterns of these two structures of *Cmcm* and *Pmma* are very similar to each other.

248   However, the intensity distributions of the reflections at low angles are different. The different volumes

249   between two octahedral sites produce an ordered structure of Ti and Fe in the sites. The site occupancy

250   analysis indicates the smaller octahedral site is occupied by Fe^{2+} and Ti is located in a larger octahedral site.

251   The bond distances indicate two crystallographically independent octahedral sites have noticeably different

252   average distances between FeO_6 and TiO_6 octahedral sites. The structure transition from *Cmcm* to *Pmma*

8

253   belongs to the order-disorder transition. Four polymorphs of Fe_2TiO_4 are presented with increasing pressure

254   in Figure 8.

255

256   X-ray emission spectra of Fe_2TiO_4 at high pressures

257   X-ray emission spectra of Fe-$K\beta$ of Fe_2TiO_4 were observed from a single-crystal Fe_2TiO_4 at high

258   pressures and room temperature. All spectra were normalized to unity for the pressure- induced shift of the

259   line maximum, based on the main fluorescence peak ($K\beta$) at 7,058 eV. Fe-$K\beta$ spectra at pressures up to

260   30.9 GPa observed at BL16-ID-B APS are shown in Figure 9. The starting material at ambient conditions

261   displays a high-spin state. With increasing pressure, the intensity of the $K\beta'$ peak decreases and the position

262   of the main $K\beta_{1,3}$ peak is shifted to lower energy to maintain the center of mass of the total $K\beta$. We applied

263   the variation of the spin state through the integrals of the integrated absolute values of the difference spectra

264   (IAD) (Vanko et al., 2006). The HS and LS spectral functions as $h(E)$ and $l(E)$ are normalized to unit area at

265   integration. The IAD value for the complete spin transition can be given as $IAD_{HL} = \int |h(E) - l(E)|\, dE$. A

266   spectrum in the transition region is a superposition of those of the two spin states, thus it can be expressed as

267    $s = \gamma_{HS}h + (1 - \gamma_{HS})l$, where γ_{HS} is the high-spin fraction. Its difference from the low-spin reference l is $s -$

268    $l = \gamma_{HS}(h - l)$. The integral of its absolute value is

269    $$IAD(s) = \int |s(E) - l(E)|\, dE = \gamma_{HS}IAD_{HL}$$

270   The IAD is proportional to a fraction of the high spin and is a good indicator of the amount of the transition.

271   The values at several pressures are shown in Figure 10. The intensity of the main peak was obtained by

272   normalization of spectra to the one center of mass of the spectra. The observed electronic spin transition

273   pressure starts at about 14 GPa. This is a very similar value to the structural transition pressure to post-spinel

274   at 15 GPa observed by XRD.

275   The peak is slightly asymmetric with a weak shoulder on the low energy side. The shoulder arises from

276   a spin flip in the metal valence shell. It has also been assigned to either plasmon excitations or

277   charge-transfer processes. Photoemission spectroscopy on free atoms shows that intra-atomic interactions

278   dominate the $K\beta$••spectral shape. $K\beta'$ and $K\beta_{1,3}$ lines move towards each other with decreasing valence

279   spin due to smaller exchange interaction between $3p$ and $3d$. The $K\beta$ merges into other weak final states on

280   the low energy side of the $K\beta_{13}$ line for S = 0. These states are due to many electron excitations where

281   additional electrons undergo a t_{2g} to e_g transition, while simultaneously a $3p$ electron decays into the $1s$

282   vacancy. This is a many-electron effect and shows the correlation in the electronic shell; upon the $3p$–$1s$

283   transition.

9

284   We observed a shift to lower energy in the $K\beta_{1,3}$ position. The $K\beta'$ peak intensity decreases a little. The

285   spin transition is an intermediate spin state in which 20 % of the total Fe transforms to low spin.

286

287   Discussion

288   The tetragonal phase of Fe_2TiO_4 with $c/a<1$ is induced from the J-T distortion by Fe^{2+} in HS state at the

289   tetrahedral site, resulting in the transformation from the cubic site symmetry of $\bar{4}3m$ to the tetragonal of

290     $\bar{4}2m$. The tetragonal distortion is enhanced with increasing pressure. The tetrahedral coordinated $Fe^{2+}(3d^6)$

291   has the electron configuration of e^3t^3 and electrons in the e orbital have a lower energy than those in the t

292   orbital. The electron spin configuration in the e orbital (double degeneracy) in the tetrahedral symmetry can

293   be distributed in either model: $(d_{x2-y2})^2(d_{z2})^1$ or $(d_{x2-y2})^1(d_{z2})^2$. In the former case, d_{x2-y2} orbital has a lower

294   energy level than d_{z2}. The present tetragonal phase prefers the former configuration under high pressure.

295   There is an obvious degradation of crystal symmetry, resulting in structural change. The electron spin state

296   yields the tetrahedral distortion with c/a<1 under high-pressure. Other three electronic spins occupy the t

297   orbital (triple degeneracy) with parallel-aligned spins and they have nothing to do with the present

298   tetrahedral distortion.

299   The distortion identified by c/a<1 is more intensively observed with increasing Ti content in the

300     $Fe_{3-x}Ti_xO_4$ solid solutions and with increasing pressure. The present J-T transition is same as our previous

301   experimental result of the J-T transition of $FeCr_2O_4$. of normal spinel structure, which is composed of Fe^{2+}

302   in the tetrahedral site (Kyono et al., 2011).

303   On the other hand, Fe_2TiO_4 transforms to the tetragonal phase with c/a>1 at low temperature below

304   -110 ℃ due to the different spin configuration from that at high pressure (Yamanaka et al., 2009). In both

305   experiments at high pressure and low temperature, c/a can be determined by spin configurations of Fe^{2+} in

306   the octahedral site. Fe^{2+} in the octahedral site has the spin configuration of $(t_{2g}^4)e_g^2$. Triple degeneracy

307   orbital t_{2g} is in lower energy level compared with e_g. One of d_{xy}, d_{yz}, and d_{zx} is an antiparallel orbit in t_{2g}.

308   However, these configurations do not lead to noticeable axial elongation or flattening of the octahedron.

309   Hence Fe^{2+} in the octahedral site do not play a significant role to produce the tetragonal distortion.

310   Electronic spin transition gives a great influence on ion radii of the transition elements, according to the

311   effective ion radii (Shannon 1976). Ion radii of Fe^{2+} at the octahedral site are r_{Fe}=0.780 Å (HS) and r_{Fe}=0.61

312   Å (LS). Ion radii are shortened in the low spin state at high pressures. The spin transition from HS to LS

313   reduces the ferrous ionic radius at the octahedral site by about 20 %. Naturally, the bond length becomes

314   shortened in the low spin state. Hence the spin transition induces the distortion of the iron sites. The

10

315   structure transition pressure of Fe_2TiO_4 to orthorhombic $CaTi_2O_4$-type is 15 GPa, but the intermediate spin

316   transition starts at about 14 GPa. On the other hand Fe_3O_4 has the post spinel structure transition pressure of

317   23 GPa and spin transition at 15 GPa (Ding et al., 2008). Our XES studies show extremely low spin

318   transition pressures compared with FeO (wüstite) and other earth iron bearing materials (Badro et al., 1999;

319   Lin et al., 2005). This is because Fe_3O_4 and Fe_2TiO_4 spinels have very short Fe-O bond distances at ambient

320   conditions, which are similar to the compressed Fe-O bond distance of many other substances under

321   extremely high-pressure condition (Table 4).

322   The present XES experiments can be interpreted by Fe^{2+} with electron configuration of $3d^6$ (e_g^2, t_{2g}^4) in

323   the octahedral site, which is more capable of causing the HS-to-LS transition compared with four-fold or

324   eight-fold coordinated sites. This is because a hybridization of d-p-π bond in the 6-fold coordination site is

325   directly transmitted by external pressure.

326   The post-spinel structure is composed of six-fold and eight-fold cation sites and shows a noticeable

327   compression of the octahedral bonds (Table 4). The spin transition promotes the compression of Fe-O

328   bonds in the octahedral site. The extremely shortened octahedral bonds induce a distortion of the eight-fold

329   cation site, which has shared edges with the octahedral site.

330   We consider the vibration of atoms under compression in order to understand the phonon-electron

331   interaction. The allowed vibrations are described by reduction into the irreducible representations of the

332   point group:

333   $\Gamma = A_{1g}+E_g +F_{1g} +3F_{2g} +2A_{2u} +2E_{2u} +5F_{1u} +2F_{2u}$ (Ishii et al., 1972; Unger et al. 1978). In our Raman

334   scattering experiment of Fe_2TiO_4 (Kyono et al., 2009), two Raman-active modes were clearly observed

335   around 500 and 700 cm^{-1}. With increasing pressure, the frequencies of the A_{1g} and F_{2g} modes increase

336   continuously up to 9 GPa with pressure derivatives of 2.5 and 2.1 cm^{-1}/GPa, respectively. At about 20 GPa,

337   the F_{2g} mode splits into $B_{1g} +E_g$ modes, and then into $B_{1g} +B_{2g} +B_{3g}$ modes. The Raman spectra are in good

338   agreement with the result from the present XRD study.

339

340   **Conclusion**

341   The present XRD and XES experiments under pressure clarify the correlation between structures and

342   spin state of $Fe_{3-x}Ti_xO_4$ solid solutions. The experimental results can be applied for the many earth materials

343   containing transition elements.

344   Rietveld structure refinements including the site occupancy determine the cation distribution of

345   $Fe_{3-x}Ti_xO_4$ solid solution. The most reliable model takes into account the crystal field instead of magnetic

346   spin ordering in the sold solution. Volume of the tetrahedral site is continuously enlarged with increasing Ti

11

347   content due to substitution of ferrous ion for ferric iron.

348   The Ti rich phase has a cubic-to-tetragonal transition under pressure by Jahn-Teller effect of $^{IV}Fe^{2+}$ ($3d^6$)

349   in the tetrahedral site. The transition pressure is lowered with Ti content. Their c/a ratios are c/a<1 due to

350   d_{x2-y2} orbital of the tetrahedral configuration, indicating c/a= 0.9787 of Fe_2TiO_4 at 11.43 GPa. XES

351   experiments prove that Fe_2TiO_4 spinel shows an extremely low spin transition pressure, because it has

352   very short Fe-O bond distances at the octahedral site even at ambient pressure. Those Fe-O bond distances

353   are similar to distances of the other substances under extremely high-pressure condition. Fe in the

354   octahedral site is more capable of causing the HS-to-LS transition, compared with the four-fold or

355   eight-fold coordinated site.

356   Transition pressure of $Fe_{3-x}Ti_xO_4$ to $CaTi_2O_4$-type structure of *Cmcm* decreases from 25 GPa (x=0.0) to

357   15 GPa (x=1.0) with increasing Ti content in the solid solution. The *Cmcm* structure of Fe_2TiO_4 is stable up

358   to 50 GPa. Octahedral bond distances in the orthorhombic post-spinel structure become noticeably

359   shortened with increasing pressure. This is because of the 20% shrinkage of ionic radius of $^{VI}Fe^{2+}$ by the

360   spin transition. Under further compression the structure transition from *Cmcm* to *Pmma* has been observed.

361   This structure change is an order-disorder transition, because the latter forms an ordered structure of Ti and

362   Fe in the octahedral site at pressures above 53 GPa.

363   The present XRD and XES experiment clarify three transitions of Fe_2TiO_4, which reflect the electronic spin

364   states due to Jahn-Teller effect on Fe^{2+} in the tetrahedral site and HS-to-IS transition of Fe^{2+} in the

365   octahedral site.

366

378

379

380

References

Akaogi, M., Hamada, Y., Suzuki, T., Kobayashi, M. and Okada, M. (1999) High-pressure transition in the system $MgAl_2O_4$-$CaAl_2O_4$: a new aluminous phase with implication for the lower mantle. Physics of the Earth and Planetary Interiors, **115**, 67-77.

Akimoto, S. (1954) Thermomagnetic study of ferromagnetic minerals contained in igneous rocks. Journal of Geomagnetism and Geoelectricity, **6**, 1-14.

Andrault, D. and Casanova, N.B. (2001) High-pressure phase transitions in the $MgFe_2O_4$ and Fe_2O_3-$MgSiO_3$ systems. Physics and Chemistry of Minerals, **28**, 211-217.

Becker, B.F. and Kasper, J.S. (1957) The structure of calcium ferrite. Acta Crystallographica, **10**,   332.

Bosi, F., Halenius, U. and Skogby, H. (2009) Crystal chemistry of the magnetite-ulvöspinel series. American Mineralogist, **94**, 181-189.

Burnley, P.C., Green, H.W., and Prior, D. (1991) Faulting Associated with the olivine to spinel transformation in Mg_2GeO_4 and its implications for deep-focus earthquakes. Journal of Geophysical Research, **96**, 425– 443.

Chevallier, R., Bolfa, J. and Mathieu, S. (1955) Titanomagnetites et ilmenites ferromagnetiques (1)   Etude optique, radio-crystallographique, chemique. Bulletin de la Société Francaise de Mineralogie et de Crystallographie, **78**, 307-346.

Dubrobinsky, L.S., Dubrovinskaia, N.A., McCammon, C., Rozenberg, G.Kh., Ahuja, R., Osorio- Guillen, J.M., Dmitriev, V., Weber, H-P., Bihan, T.Le. and Johansson, B. (2003) The structure of the metallic high-pressure Fe_3O_4 polymorph: experimental and theoretical study. Journal of Physics: Condensed Matter, **15,** 7697-7706

Fei, Y., Mao, H., Hemley, R., Shu, J.F. and Shen, G. (1999) In situ structure determination of the high-pressure phase of Fe_3O_4. American Mineralogist, **84**, 203-206.

Finger, L.W., Hazen R.M. and Hofmeister, A.M. (1986) High-pressure crystal chemistry of spinel ($MgAl_2O_4$) and magnetite (Fe_3O_4): comparison with silicate spinels. Physics and Chemistry of Minerals, **13**, 215–220.

Forster, R.H. and Hall, E.O. (1965) A neutron and X-ray diffraction study of ulvöspinel, Fe_2TiO_4.   Acta Crystallographica, **18**, 859-862.

Funamori, N., Jeanloz, R., Nguyen, H., Kavner, A. and Caldwell, W.A. (1998) High-pressure transformation in $MgAl_2O_4$. Journal of Geophysical Research, **103**, 20813-20818.

Geisber, H.G., Pennington, W.T. and Kolis, J.W. (2001) Redetermination of $CaMn_2O_4$. Acta Crystallographica, C **57**, 329-330.

14

413 Haavik, C., Tolen, S., Fjellvag, H., Hanfland, M. and Hauserman, D. (2000) Equation of sate of magnetite

414 and its high-pressure modification: thermodynamics of Fe-O system at high pressure. American

415 Mineralogist, **85**, 514-523.

416 Harrison, R.J., Dove, M.T., Knight, K.S. and Putnis, A. (1999) In situ neutron diffraction study of

417 non-convergent cation ordering in the $(Fe_3O_4)_{1-x}(MgAl_2O_4)_x$ spinel solid solution. American Mineralogist,

418 **84**, 555-563.

419 Honig, M. and Aragon, R. (1986) Equilibrium oxygen fugacity in titanium ferrite. Zeitschrift fur

420 Anorganische und Allegemeine Chemie, **541**, 80-90.

421 Huang, E. and Bassett, W.A. (1986) Rapid determination of Fe_3O_4 phase diagram by synchrotron radiation.

422 Journal of Geophysical Research, **91**, 4697-4703

423 Irifune, T., Fujino, K. and Ohtani, K. (1991) A new high-pressure form of $MgAl_2O_4$. Nature, **349**, 409-411.

424 Ishii, M., Nakahira, M. and Yamanaka, T. (1972) Infrared absorption spectra and cation distribution in (Mn,

425 Fe)$_3$O$_4$. Solid State Communication. **11**, 209-212

426 Izumi, F. and Ikeda, T. (2000) A Rietveld-analysis program RIETAN-98 and its applications to zeolites.

427 European Powder Diffraction, Materials Science Forum, 198-203.

428 Kakol, Z., Sabol, J., Stikler J. and Honig, J.M. (1992) Cation distribution and magnetic properties of

429 titanomagnetites $Fe_{3-x}Ti_xO_4$ (0<x<1.0). Physical Review, B. **43,** 649.

430 Kuriki, A., Moritomo, Y., Ohishi, Y., Kato, K., Nishibori, E., Takata, M., Sakata, M., Hamada, N., Todo, S.,

431 Mori, N., Shimomura, O. and Nakamura, A. (2002) High-pressure structural analysis of Fe_3O_4. Journal

432 Physical Society of Japan, **71**, 3092–3093

433 Kyono, A., Ahart, M., Yamanaka, T., Gramsch, S., Mao, H.K. and Hemley, R.J. (2011)   High- pressure

434 Raman spectroscopic studies of ulvöspinel Fe_2TiO_4. American Mineralogist, **96**, 1193-1198.

435 Kyono, A., Gramsch, S.A., Yamanaka, T., Ikuta, D., Ahart, M., Mysen, B.O., Mao, H.K. and   Hemley,

436 R.J. (2011) The influence of the Jahn–Teller effect at Fe^{2+} on the structure of chromite at high pressure.

437 Physics and Chemistry of Minerals, DOI 10.1007/s00269-011-0468-6.

438 Lindsley, D.H. (1976) The crystal chemistry and structure of oxide minerals as exemplified by the Fe-Ti

439 oxides in D. Rumble, Ed., Mineralogical Society of America: Short Course Notes 3, p. L-1-60.

440 Mineralogical Society of America, Chantilly, Virginia.

441 Mao, H.K., Takahashi, T., Bassett, W.A., Kinsland, G.J. and Merril, L. (1974) Isothermal compression of

442 magnetite to 320 kbar and pressure-induced phase transformation. Journal of Geophysical Research,

443 **79**,1165-1170

444 Mao, H.K., Xu, J. and Bell, P.M. (1986) Calibration of the ruby pressure gauge to 800-kbar under quasi-

15

445   hydrostatic conditions. Journal Geophysical Research, **91**, 4673- 4676.

446   Méducin, F., Redfern, S.Q.T., Godec, Y.L., Stone, H.J., Trucker, M.G., Dove, M.T. and Marshall, Z.G.

447   Study of cation order-disorder in $MgAl_2O_4$ spinel by in situ neutron diffraction up to 1600 K and 3.2 GPa.

448   American Mineralogist, **89**, 981-986.

449   Nakagiri, N., Manghnani, M.H., Ming, L.C. and Kimura, S. (1986) Crystal structure of magnetite under

450   pressure. Physics Chemistry of Minerals, **13**, 238-244.

451   Neel, L. (1955) Some theoretical aspects of rock magnetism. Advances in Physics, **4**, 191-243.

452   O'Reilly, W. and Banerjee, S.K. (1965) Cation distribution in titanomagnetites $(1-x)Fe_3O_4 - xFe_2TiO_4$.

453   Physics Letters, **17**, 237-238.

454   Pasternak, M.P., Nasu, S., Wada, K. and Endo, S. (1994) High-pressure phase of magnetite. Physical

455   Review, B **50**, 6446-6449.

456   Pearce,C.T., Henderson, C.M., Pattrick, R.A.D., vander Laan, G., Vaughan, D.J. (2006) Direct

457   determination of cation site occupancies in natural ferrite spinels by $L_{2,3}$ X-ray absorption spectroscopy and

458   X-ray magnetic circular dichroism. American Mineralogist, **91**, 880-893.

459   Piermarini, G.J., Blook, S., Barnett, J.D. and Forman, R.A. (1975) Calibration of the pressure dependence

460   of the R1 ruby fluorescence line to 195 kbar. Journal of Applied Physics, **46**, 2774-2780.

461   Reid, A.F. and Ringwood, A.E. (1969) Newly observed high-pressure transformations in Mn_3O_4, $CaAl_2O_4$

462   and $ZrSiO_4$. Earth and Planetary Science Letter, **6**, 205-208.

463   Reichmann, H.J. and Jacobsen, S.D. (2004) High-pressure elasticity of a natural magnetite crystal.

464   American Mineralogist, **89**, 1061-1066.

465   Rogge, M.P., Caldwell, J.H., Ingram, D.R., Green, C.E., Geselbracht, M.J. and Siegrist, T. (1998) A new

466   synthetic route to pseudo-brookite-type $CaTi_2O_4$. Journal of Solid State Chemistry, **141**, 338-342.

467   Rozenberg, G,Kh., Amiel, Y., Xu, W.M., Pasternak, M.P., Jeanloz, R., Hanfland, M. and Taylor,   R.D.

468   (2007) Structural characterization of temperature- and pressure-induced inverse normal spinel

469   transformation in magnetite. Physical Review B **75**, 020102—4.

470   Rueff, J.P., Ka, C.C., Struzhkin, V.V., Badro, J., Shu, J.F., Hemley, R.J. and Mao, H.K. (1999)

471   Pressure-induced high-spin to low-spin transition in FeS Evidenced by X-ray emission spectroscopy.

472   Physical Review Letter, **82**, 3284-3287.

473   Shannon, R.D. (1976) Revised effective ionic radii and systematics of interatomic distances in halides and

474   chalcogenides. Acta Crystallographica, A **32**, 751-767.

475   Todo, S., Takeshita, N., Kanehara, T., Mori, T. and Mori, N. (2001) Metallization of magnetite (Fe_3O_4)

476   under high-pressure. Journal Applied Physics, **89**, 7347–7349.

16

477   Unger, W.K., Farnworth, B., and Irwin, J.C. (1978) Raman and infrared-spectra of $CdIn_2S_4$ and $ZnIn_2S_4$.

478   Solid State Communications, **25**, 913–915.

479   Vanko, G., Neisius, T., Molna´r, G., Renz,| F., Ka´rpa´t, S., Shukla,, A and de Groot, F.M.F. (2006)

480   Probing the 3d spin momentum with X-ray emission spectroscopy: The case of molecular-spin Transitions.

481   Jour. Physical Chemistry B **110**, 11647-11653.

482   Waskowska, A., Gerward, L., Olsen, S.J., Steenstrup, S. and Talik, E. (2001) $CuMn_2O_4$: properties and the

483   high-pressure induced Jahn-Teller phase transition. Journal of Physics: Condensed Mater, **13**, 2549-2562.

484   Wechsler, B.A., Lindsley, D.H. and Prewitt, C.T. (1984) Crystal structure and cation distribution in

485   titanomagnetes ($Fe_{3-x}Ti_xO_4$). American Mineralogist, **69**, 754-770.

486   Yamanaka, T. and Okita, M. (2001a) Magnetic Properties of the Fe_2SiO_4-Fe_3O_4 spinel solid solution.

487   Physics and Chemistry of Minerals, **28**, 102-109.

488   Yamanaka, T., Shimazu, H. and Ota, K. (2001b) Electric Conductivity of the Fe_2SiO_4-Fe_3O_4 spinel solid

489   solution. Physic and Chemistry of Minerals, **28**,110-118.

490   Yamanaka, T., Uchida, A. and Nakamoto, Y. (2008) Structural transition of post-spinels, $CaTi_2O_4$,

491    $CaMn_2O_4$ and $CaFe_2O_4$ under high pressures up to 80 GPa. American Mineralogist, **93,** 1874-1881.

492   Yamanaka, T., Mine, T., Asogawa, S. and Nakamoto, Y. (2009) Jahn-Teller transition of Fe_2TiO_4 observed

493   by Maximum Entropy Method at high-pressure and low Temperature. Physical Review B **80**, 134120.

494   Zinii, P., Tatsumi-Petrochios, L., Bonal, L., Acosta, T., Hamer, J., Gilder, A. and Fuller, M. (2011) Raman

495   spectroscopy of titanomagnetites: Calibration of the intensity of Raman peaks as a sensitive indicator for

496   their content. American Mineralogist, **96,** 1537-1546.

497

17

498   **Figure caption**

499   Figure 1.   Bond distance and site volume as a function of composition.

500   A-O and B-O indicate the bond distance of the tetrahedral and octahedral site.

501   Solid circles and star symbol indicate the reflections of the orthorhombic and new

502   phase.

503   Figure 2.   Pressure dependence of the lattice constant of $Fe_{3-x}Ti_xO_4$ spinel solid solutions.

504   The lattice constant of each spinel phase shows a monotonous change in the high-

505   pressure region.

506   Figure 3.   Lattice constants of the cubic and tetragonal phases of x=0.831 and x=1.0 in

507               $Fe_{3-x}Ti_xO_4$.

508   Figure 4   Rietveld profile fitting of the high-pressure phase of Fe_2TiO_4 at 40GPa.

509   Initial model for the profile fitting is the $CaTi_2O_4$ structure with *Cmcm*.

510   Figure 5   High-pressure structure of Fe_2TiO_4 with *Cmcm*.

511   One of Fe^{2+} occupies M1 site and the other M2 site. Ti^{4+} and Fe^2 disorderly occupy the

512   M2 site.

513   Figure 6   Rietveld profile fitting of the high-pressure phase of Fe_2TiO_4 at 61 GPa.

514   Initial model for the profile fitting is the $CaTi_2O_4$ structure with *Pmma*

515   Figure 7   Structure of Fe_2TiO_4 at 61 GPa with *Pmma*.

516   Figure 8   Unit cell volumes of four high-pressure polymorphs of Fe_2TiO_4.

517   The unit cell volume of the cubic phase is presented by half of the true value in order

518   to normalize all four polymorphs.

519   Figure 9   X-ray emission spectra of Fe-$K\beta$ in Fe_2TiO_4 at increasing pressure up to 30.9 GPa.

520   The spectra collected from a single-crystal Fe_2TiO_4 at high pressures and room

521   temperature. The upper left figure sows the expanded $K\beta$ spectra, indicating an

522   intermediate spin transition. The transition starts from 14 GPa. Intermediate spin

523   electron increases with pressure.

524   Figure 10   Relative integrated intensities due to energy shift of Fe-$K\beta$.

525   The integrated absolute differences (IAD) between spectra at indicated pressures

526   and the spectrum at highest pressure, 30.9 GPa. The IAD is proportional to a fraction

527   of the high spin. The significant reduction of the IAD after 14 GPa correlates with the

528   structural transition found in Fe_2TiO_4 at 15 GPa. The scale of vertical axis is

18

529   introduced by the equation indicating the variation of the spin state through the

530   integrals of the absolute values (see text).

531

532   Tables.

533   Table 1   Lattice constant of $Fe_{3-x}Ti_xO_4$ spinels under high pressure.

534   Data with a mark of * belong to the tetragonal spinel.

535   Samples of x= 0.734, 0.831 and 1.0 show the tetragonal lattice constants a and c are

536   also presented together with c/a ratio. a of the tetragonal phase is presented by $\sqrt{2}$ time

537   of a. The number of parenthesis is the error of the last decimal.

538   Table 2   Bulk modulus of the spinel $Fe_{3-x}Ti_xO_4$ phase.

539   Ko* is calculated with fixed Ko'=4. R indicates the goodness factor for the fitting.

540   Table 3   Structure of four high-pressure polymorphs of Fe_2TiO_4.

541   Results of structure data at 14, 50 and 61 GPa are from the Rietveld profile fitting of powder

542   diffraction data. The definitions of the reliability factors R_F, R_I, R_P, wR_P and goodness of fit s in

543   the refinement are

$$R_F = \left[\frac{\sum_k |F_{k\ obs}| - |F_{k\ cal}|}{\sum_k F_{k\ obs}} \right] , \quad R_I = \left| \frac{\sum_i |I_{i\ obs} - I_i(x)|}{\sum_i I_{i\ obs}} \right| ,$$

$$R_p = \left[\frac{\sum_i |y_i - f_i(x)|}{\sum_i y_i} \right] , \quad wR_p = \left[\frac{\sum_i w_i |y_i - f_i(x)|}{\sum_i w_i y_i} \right]^{1/2} , \quad s = \left[\frac{\sum_i w_i |y_i - f_i(x)|}{N - P} \right]^{1/2} ,$$

546   where I indicates the integrated intensity of diffraction peak, y_i is the observed diffraction

547   intensity at i-th position in 2θ, $f(x)$ is the calculated intensity. N and P indicate the total number of

548   the data point and variable parameters, respectively.

549   Structure at 5.58 GPa is observed from the single crystal diffraction study.

550   Table 4   Lattice constant and bond distance of four high-pressure polymorphs of Fe_2TiO_4:

551   cubic, tetragonal and two orthorhombic phases.

552   Data of 61* are based on the *Cmcm* structure and presented for comparison sake to the
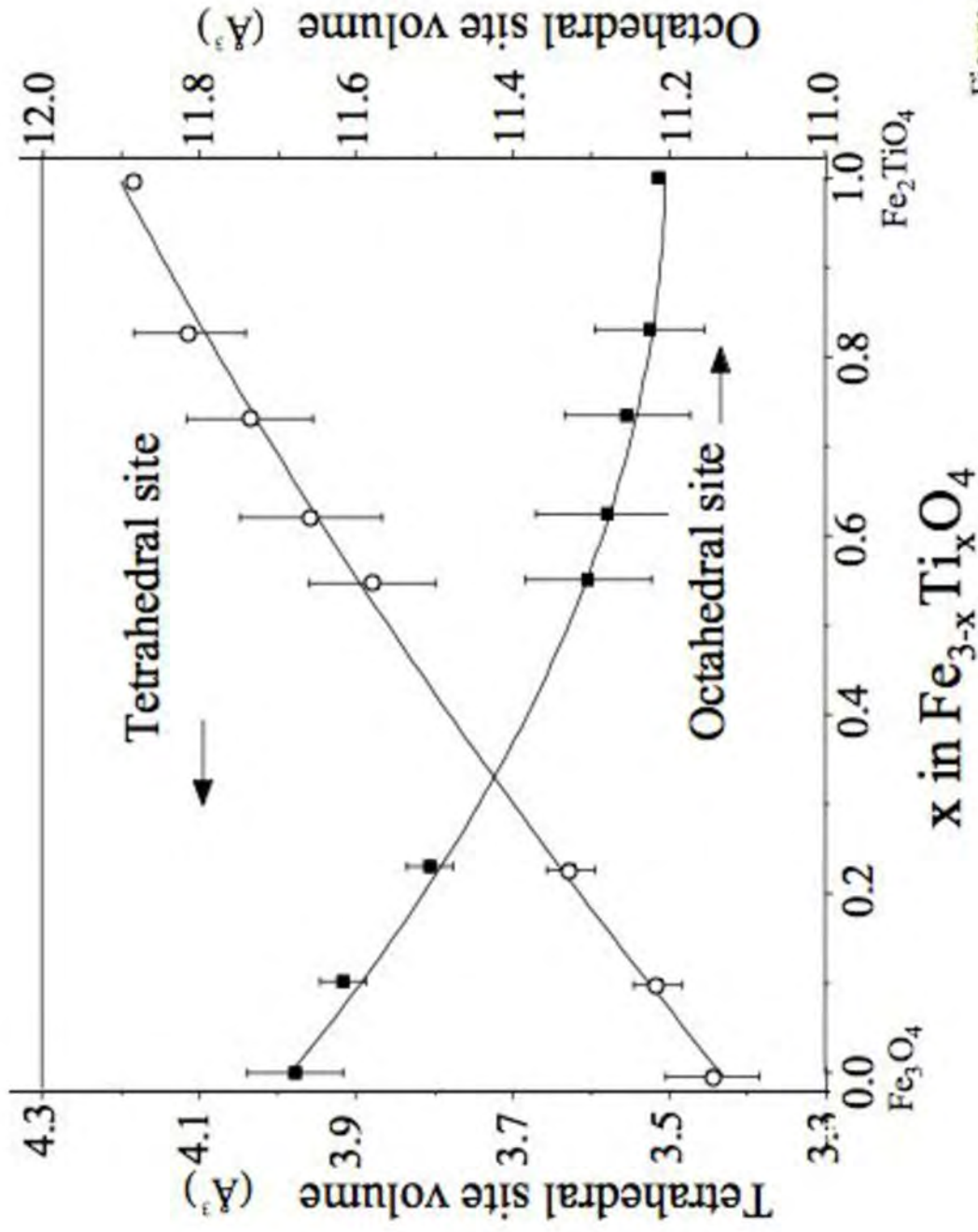
553   result of the *Pmma* structure.

19

Figure 1
Yamanaka

Figure 2
Yamanaka

Figure 3
Yamanaka

M1: Fe^{2+}

M2: $Fe^{2+} + Ti^{4+}$

O^{2-}

Fe

Fe + Ti

O

Figure 4
Yamanaka

Figure 5
Yamanaka

Fe$_2$TiO$_4$ 61 GPa *Pmma*
R$_I$= 0.190 R$_F$=0.249

2 θ (λ=0.42189 Å)

Figure 6
Yamanaka

Fe₂TiO₄ 61 GPa *Pmma*

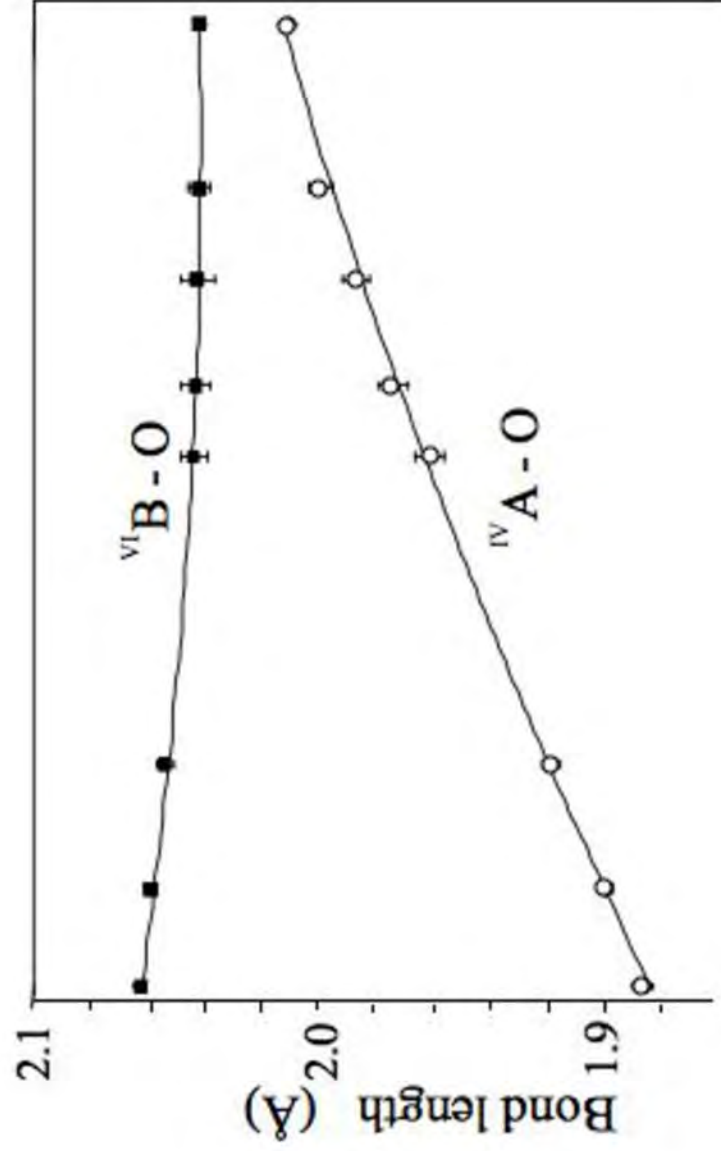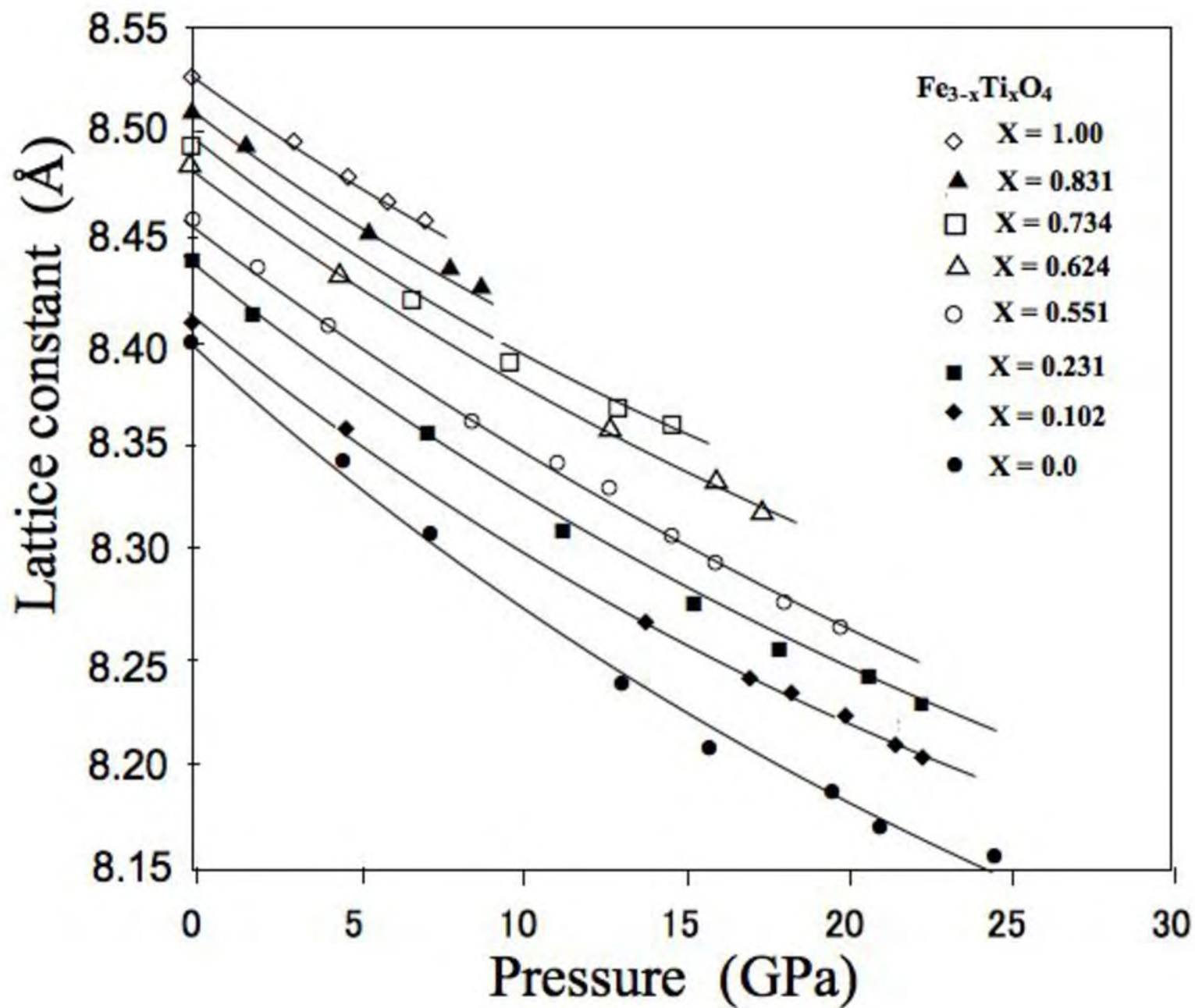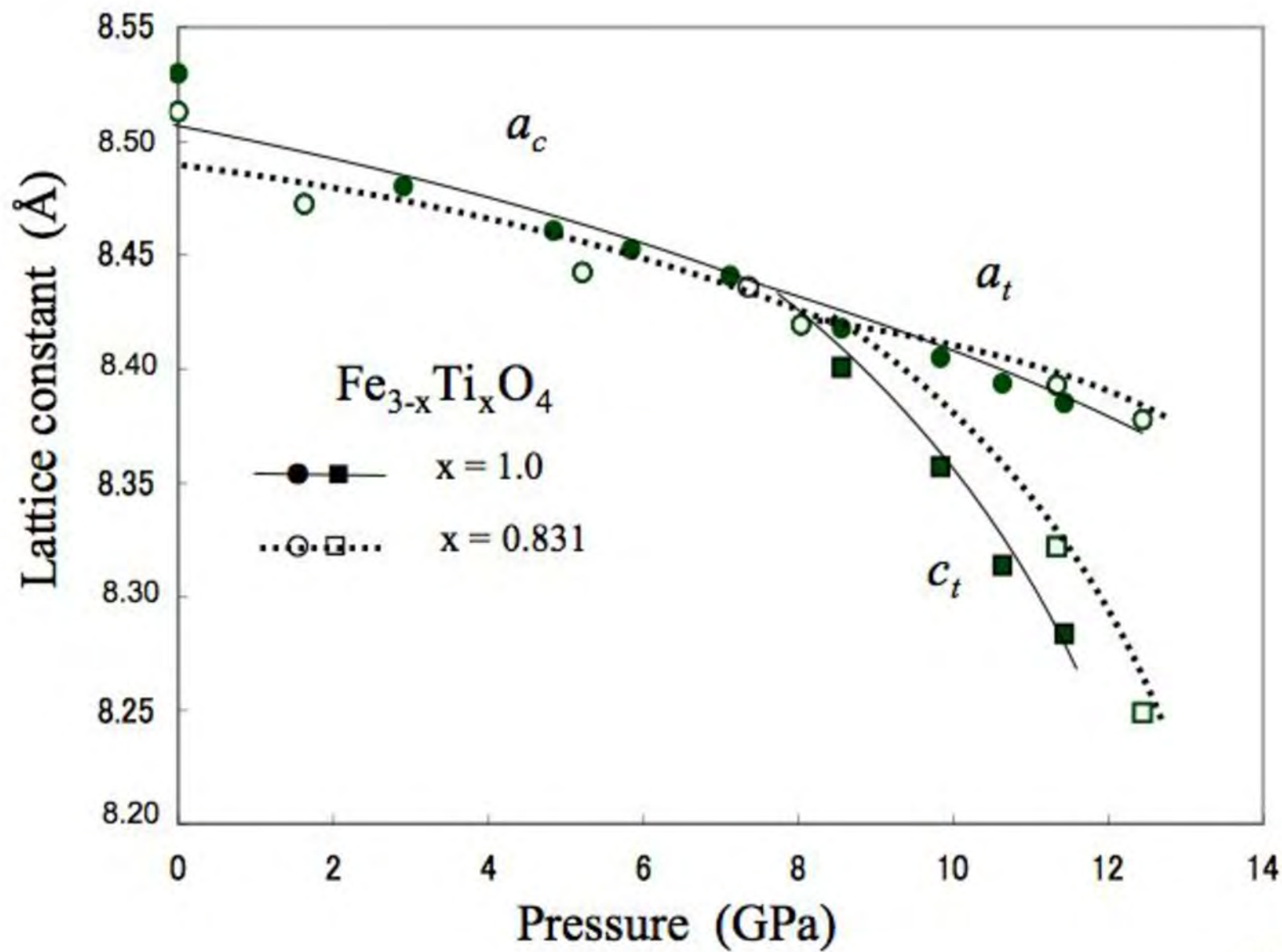Fe (high spin) in 8-fold

Fe (low spin) in 6-fold
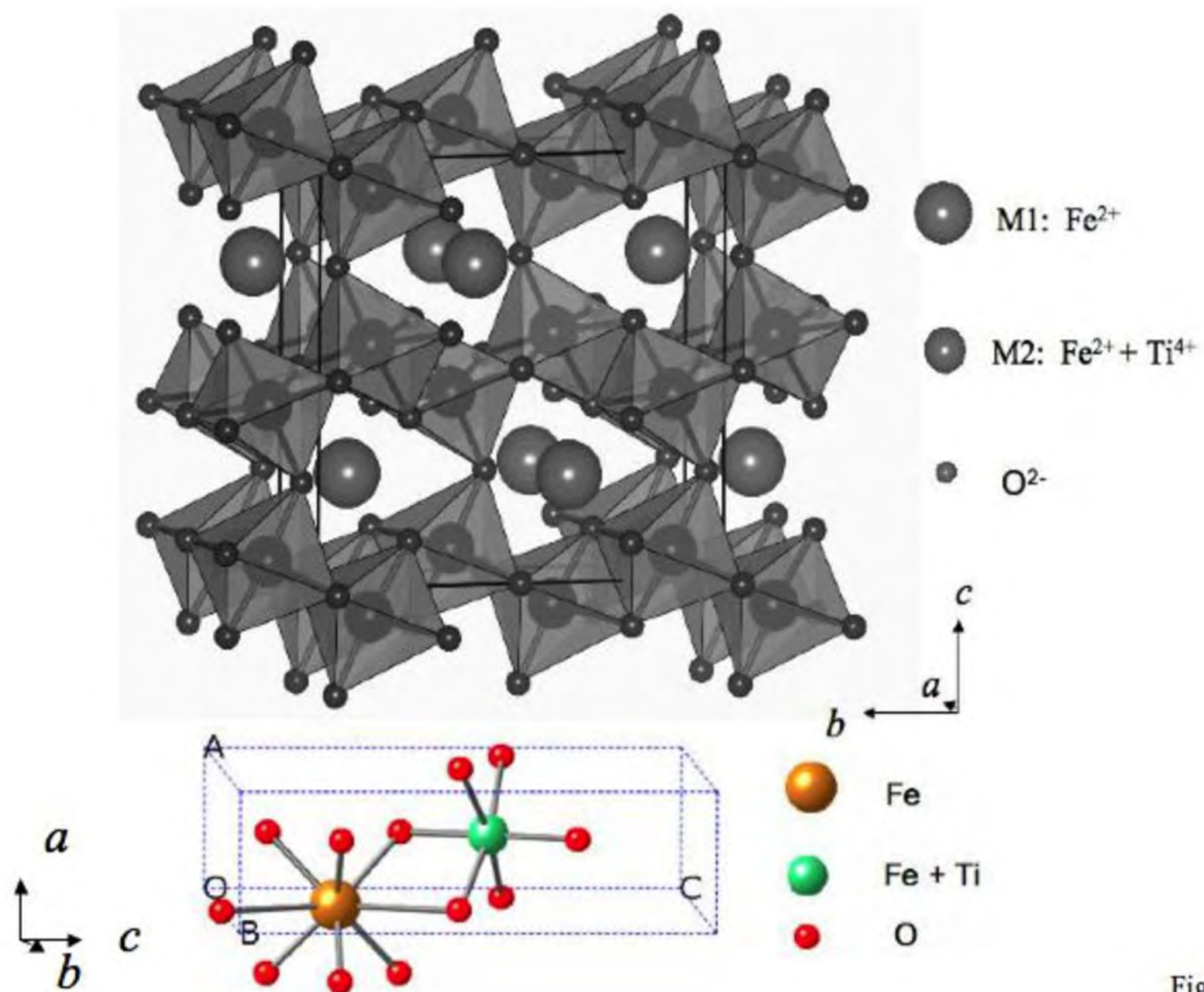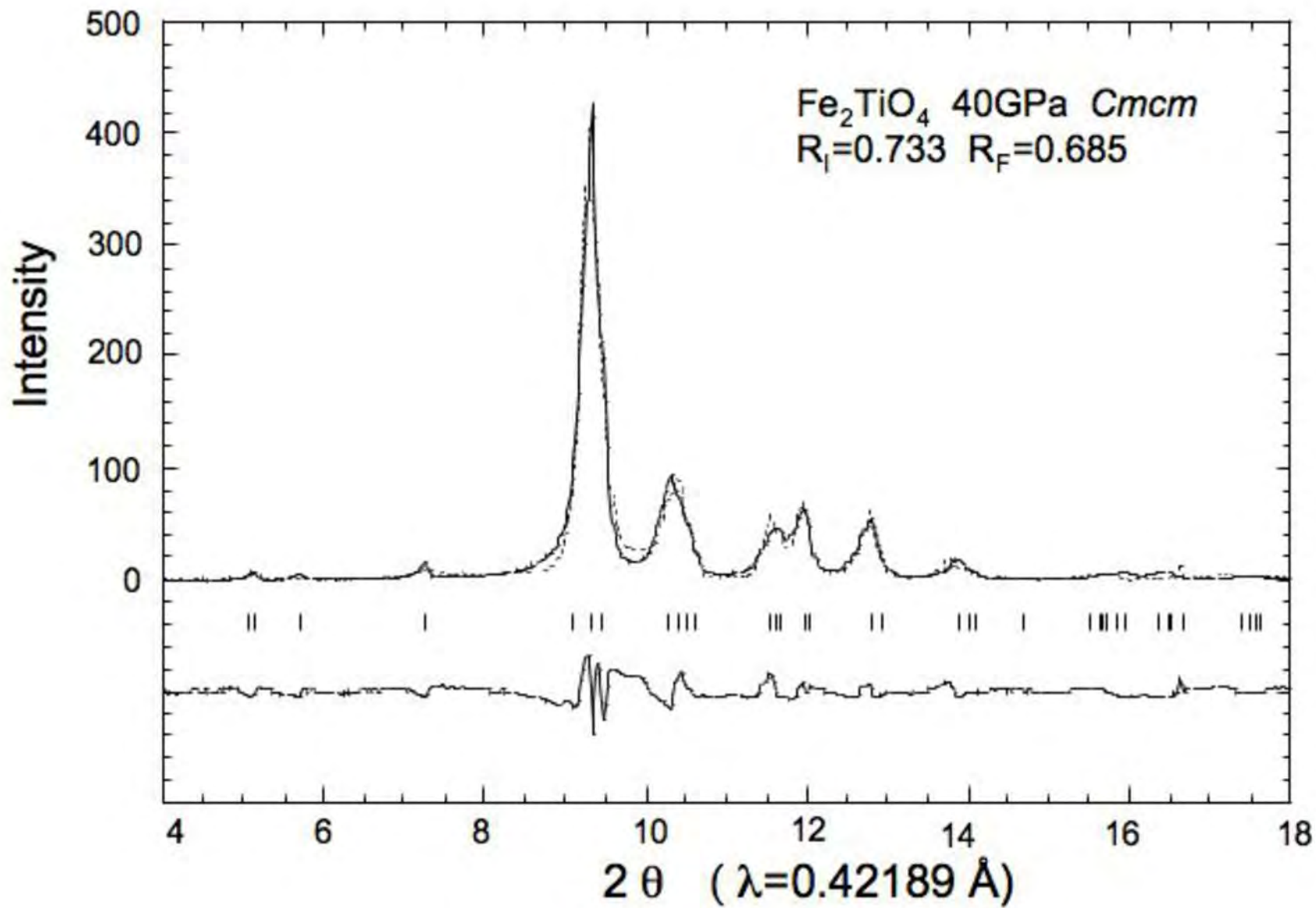
Ti in 6-fold
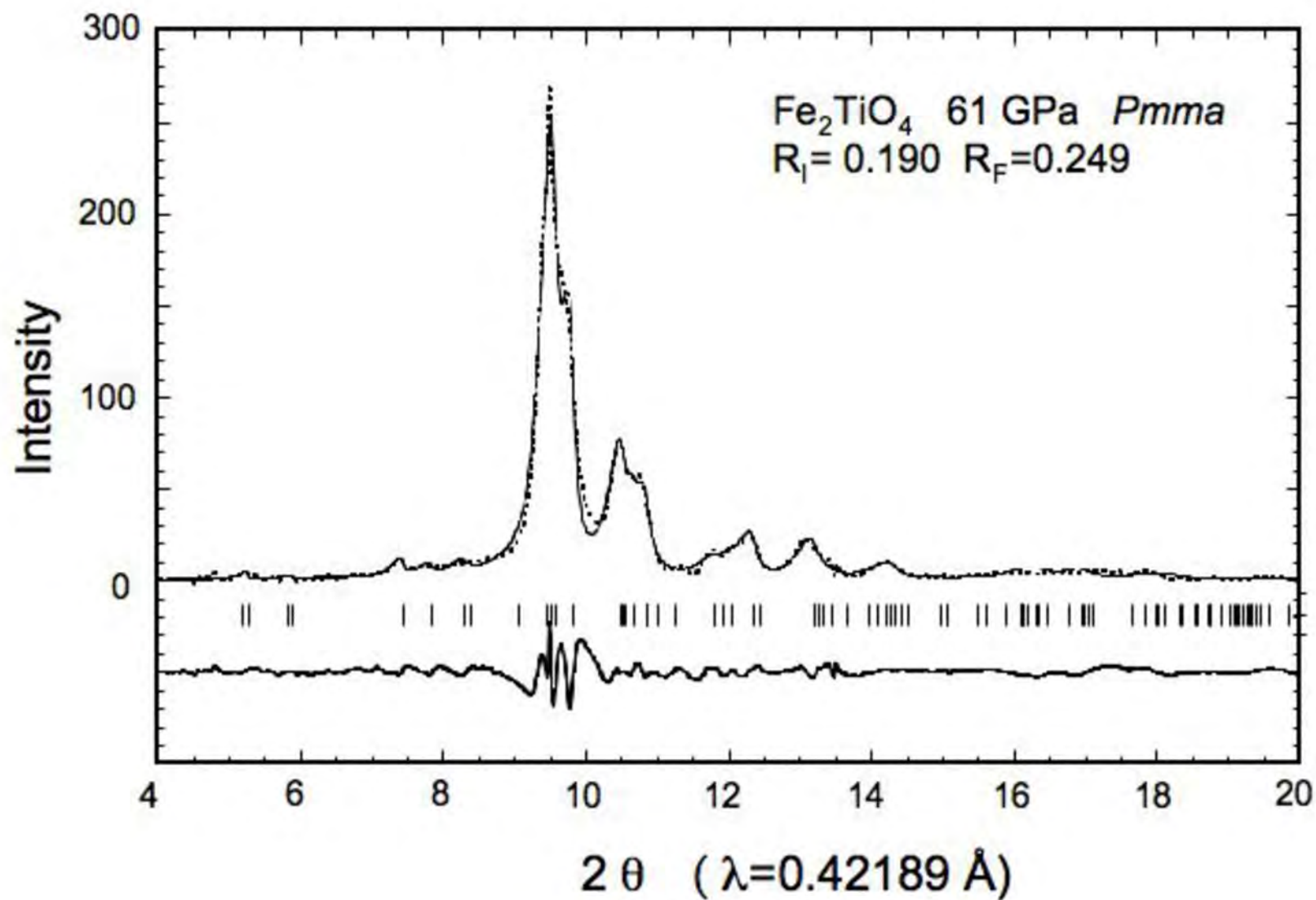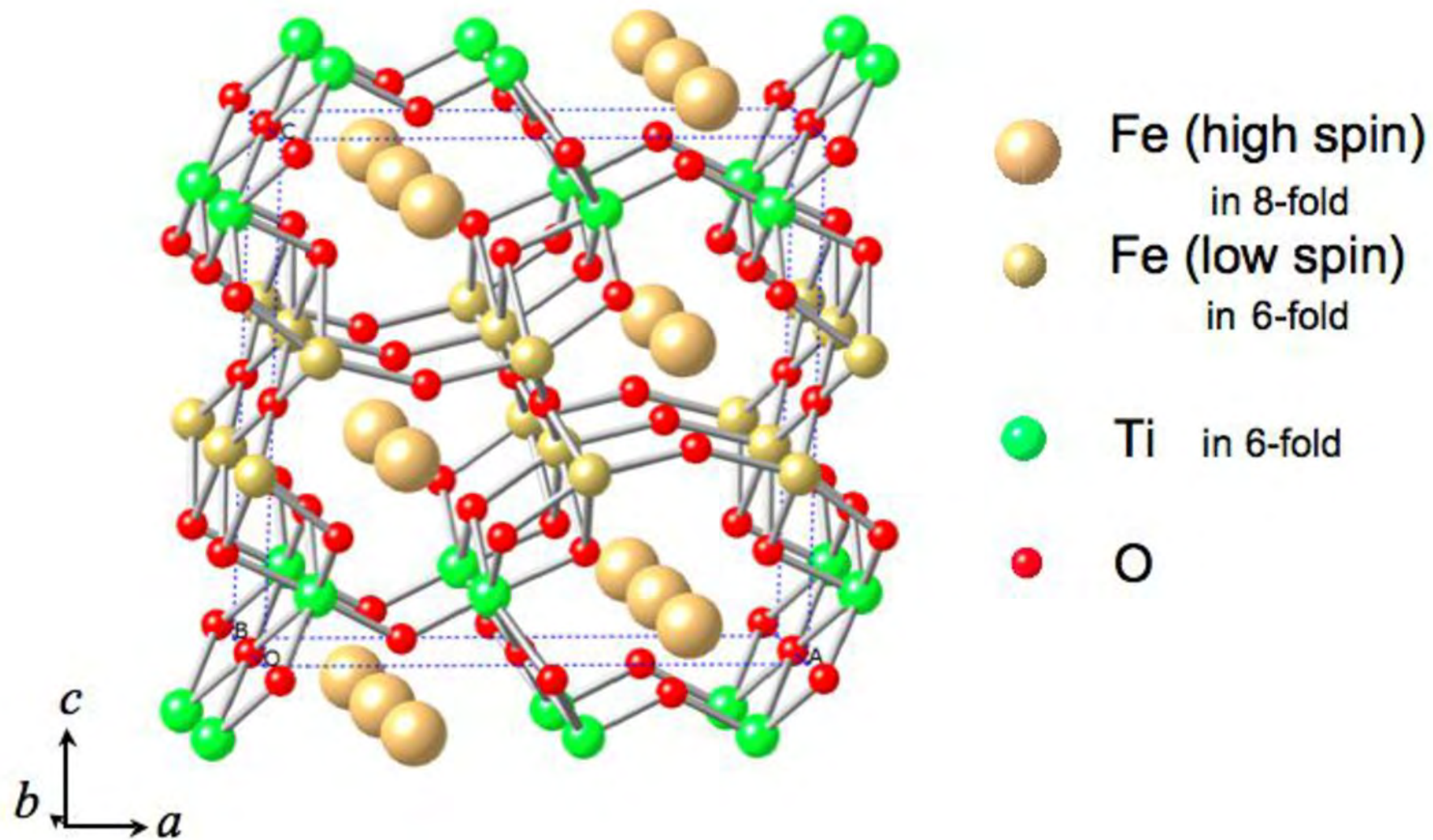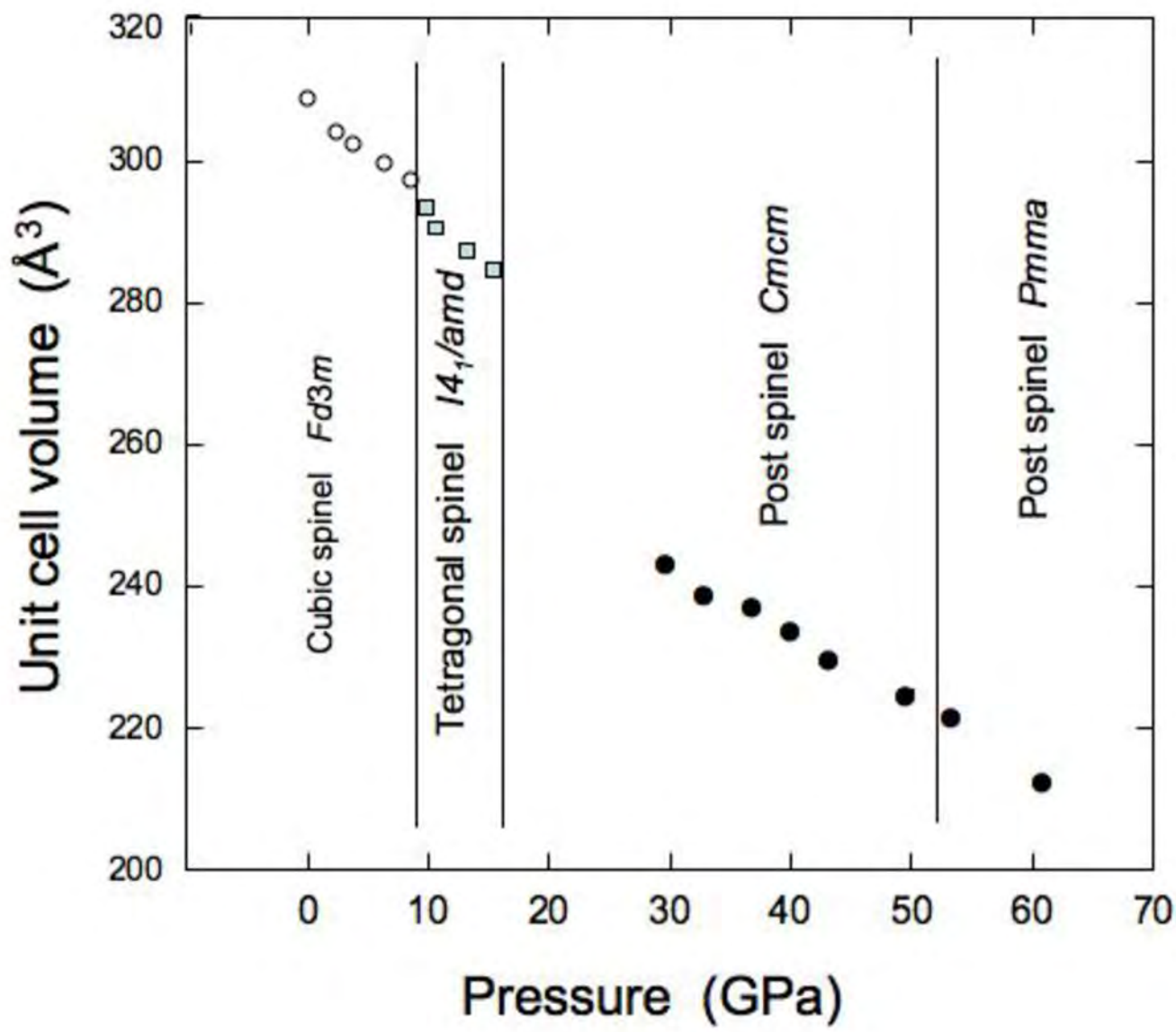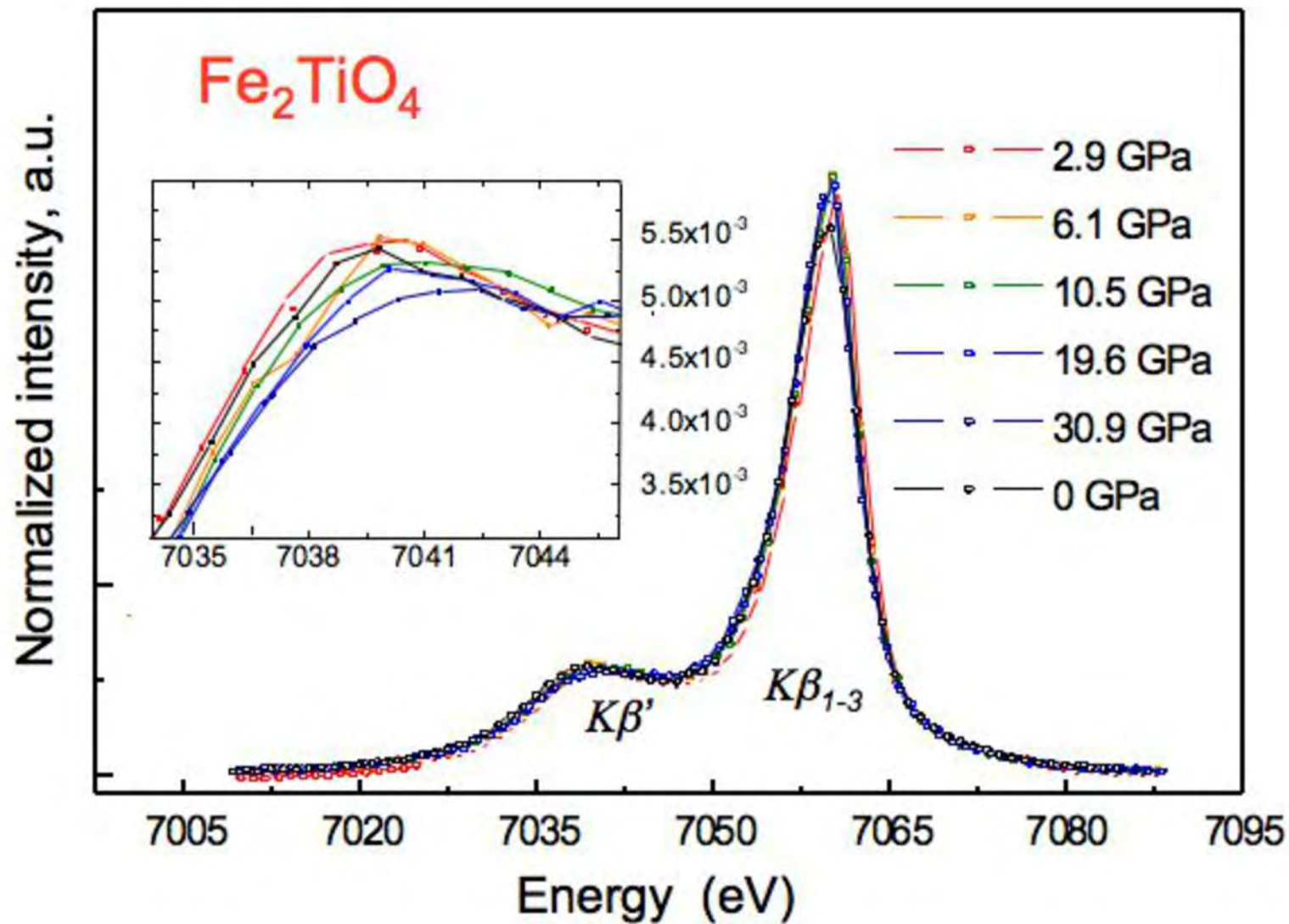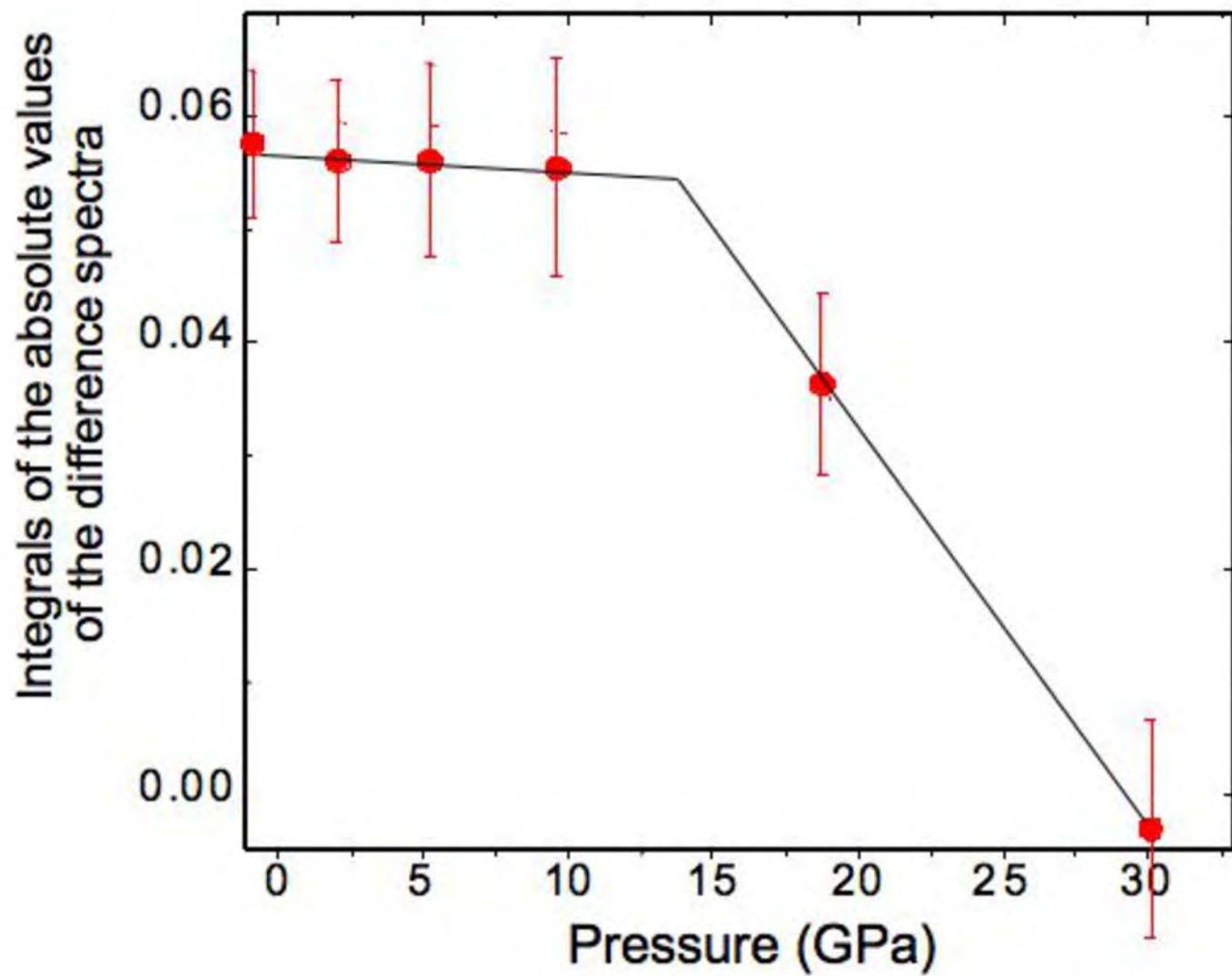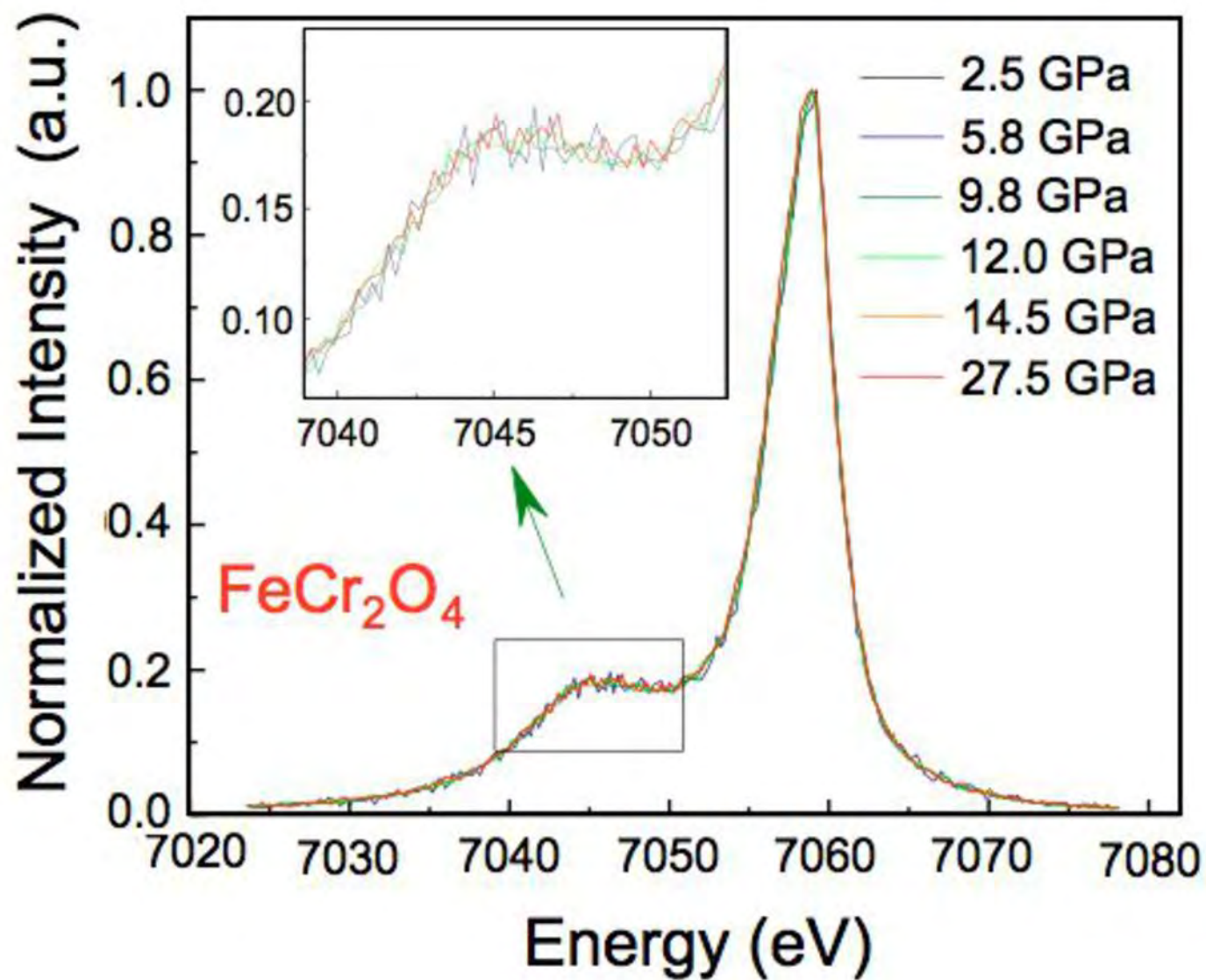
O

Figure 7
Yamanaka

Figure 8
Yamanaka

Figure 9
Yamanaka

Figure 10
Yamanaka

Figure 11
Yamanaka

Table 1.
Lattice constant of $Fe_{3-x}Ti_xO_4$ spinel solid solution under high pressure

x=0.0		x=0.102		x=0.231		x=0.551		x=0.624	
P(GPa)	a (Å)	P(GPa)	a (Å)	P(GPa)	a (Å)	P(GPa)	a (Å)	P(GPa)	a (Å)
0.0001	8.3984(8)	0.0001	8.4102(9)	0.0001	8.4241(10)	0.0001	8.4632(7)	0.0001	8.4802(10)
4.63	8.3488(6)	4.69	8.3637(8)	2.099	8.4146(7)	2.02	8.4360(9)	4.40	8.4298(11)
7.06	8.3158(8)	13.83	8.2757(10)	6.99	8.3561(6)	4.12	8.4092(11)	12.5	8.3645(14)
12.29	8.2491(11)	16.99	8.2444(12)	11.45	8.3041(9)	8.62	8.3652(13)	15.9	8.3350(9)
16.51	8.2152(9)	17.95	8.2358(9)	15.43	8.2763(10)	11.23	8.3414(18)	17.3	8.3225(14)
19.1	8.1864(5)	19.88	8.2276(10)	17.98	8.2582(15)	12.54	8.3277(13)		
21.75	8.1708(7)	21.83	8.2193(8)	21.17	8.2448(12)	14.60	8.3059(17)		
24.69	8.1601(7)	22.74	8.2101(9)	22.10	8.2292(13)	16.05	8.2937(9)		
						17.84	8.2759(14)		
						19.54	8.2613(21)		

X=0.734				x=0.831				x = 1.0			
P(GPa)	a (Å)	c (Å)	c/a	P(GPa)	a (Å)	c (Å)	c/a	P(GPa)	a (Å)	c (Å)	c/a
0.0001	8.4969(6)			0.0001	8.5131(7)			0.0001	8.5297(4)		
6.63	8.4228(7)			1.63	8.4939(12)			2.91	8.4974(9)		
9.88	8.3908(10)			5.22	8.4535(9)			4.84	8.4768(11)		
12.62	8.3724(8)			7.54	8.4333(10)			5.84	8.465011)		
14.65	8.3644(8)			8.04	8.4259(17)			7.12	8.45513(9)		
*16.30	8.3657(9)	8.3550(9)	0.99987	*11.34	8.3928(8)	8.3218(17)	0.9915	*8.56	8.4178(12)	8.4004(14)	0.9980
				*12.45	8.3775(10)	8.2488(20)	0.9846	*9.83	8.4048(12)	8.3567(14)	0.9942
					*			*10.64	8.3934(14)	8.3136(18)	0.9905
								*11.43	8.3857(12)	8.2836(16)	0.9878

Table 2

Bulk modulus of the spinel $Fe_{3-x}Ti_xO_4$ phase.

X	Ko (GPa)	Ko'	R	Ko*(GPa)	No of data
0	183.4 (8.1)	7,1 (2.9)	0.9959	220.4 (4.6)	8
0.102	207.7 (14.8)	8.9 (3.4)	0.9977	263.4 (4.3)	8
0.231	224.3 (10.4)	7.9 (3.4)	0.9982	269.3 (5.1)	8
0.551	226,8 (6.3)	5.7 (2.3)	0.9995	232.8 (1.3)	10
0.624	237.9 (14.4)	6.3 (7.3)	0.9995	275.2 (5.6)	5
0.734	228.9 (0.6)	5.3 (0.1)	0.9999	246.3 (2.2)	5
0.831	227.7 (4.5)	6.7 (1.5)	0.9999	242.4 (1.9)	5
1.000	238.1 (4.2)	7.6 (2.4)	0.9994	250.8 (2.5)	5

Table 3　　Result of the Rietveld profile fitting of high-pressure phase of Fe_2TiO_4

7GPa　Cubic spinel　$Fd3m$　z=8　　a=8.521(2)Å　b=8.521(2)Å　c=8,521(3)Å

Atom	Wyck.	site sym.	multiplicity	occupancy	x	y	z
Fe1	8a	$4\bar{3}m$	0.25	8	0.0	0.0	0.0
Ti+Fe2	16d	$.\,\bar{3}m$	0.50	16	0.625	0.625	0.625
O1	32e	..3m	1.0	32	0.3629(9)	0.3629(9)	0.3629(9)

R_I=1.652　　R_F=2.557　　R_P=0.557　　wR_P=1.072　　s=0.1626

14GPa　Tetragonal Spinel　$I4_1/amd$　z=4　　a=5.985(8)Å　b=5.985(8)Å　c=7.999(10)Å

Atom	Wyck.	site sym.	multiplicity	occupancy	x	y	z
Fe1	4b	$\bar{4}m2$	0.25	4	0.0	0.0	0.5
Ti+Fe2	8c	.2/m.	0.50	8	0.0	0.75	0.125
O	16h	.m.	1.0	16	0.0	0.1293(6)	0.282(6)

R_I =9.163　　R_F=6.730　　R_P=1.126　　wR_P=2.341　　s=0.1626

50GPa　$Cmcm$　z=4　a=2.685(7)Å　　b=9.228(3)Å　c=9.099(3)Å　　Vol=225.5(9) Å³

Atom	Wyck.	site sym.	multiplicity	occupancy	x	y	z
Fe1	4c	m2m	0.5	4	0.0	0.396(1)	0.25
Ti +Fe2	8f	m..	1.0	8	0.0	0.133(1)	0.068(1)
O1	4b	2/m..	0.5	4	0.0	0.109(2)	0.25
O2	8f	2/m..	1.0	8	0.0	0.261(1)	0.623(2)
O3	4b	m..	0.5	4	0.0	0.5	0.0

R_I =0.365　　R_F =0.345　　R_P =0.365　　wR_P =0.628　　s=0.1626

61GPa　$Pmma$　z=4　a=9.059(8)Å　b=2.659(4)Å　c=9.166(7)Å　Vol=220.7(9) Å³

Atom	Wyck.	site sym.	multiplicity	occupancy	x	y	z
Fe1	2e	mm2	0.5	2	0.25	0.0	0.392(1)
Fe2	2f	mm2	0.5	2	0.25	0.5	0.899(1)
Fe3	41	.m.	1.0	4	0.090(3)	0.0	0.136(2)
Ti	4j	.m.	1.0	4	0.057(7)	0.5	0.610(2)
O11	2c	.2/m.	0.5	2	0.0	0.0	0.5
O12	2b	.2/m	0.5	2	0.0	0.5	0.0
O21	2e	mm2	0.5	2	0.25	0.5	0.561(5)
O22	2f	mm2	0.5	2	0.25	0.0	0.051(5)
O31	4i	.m.	1.0	4	0.400(9)	0.5	0.272(3)
O32	4j	.m.	1.0	4	0.418(6)	0.0	0.783(4)

R_I =0.190　　R_F =0.249　　R_P =0.308　　wR_P =0.545　　s=0.11354

Table 4   Bond distance of Fe_2TiO_4 as a function of pressure

	Single crystal structure analysis				Rietveld profile fitting analysis						
	Cubic (*Fd3m*)		Tetragonal (*I4₁/amd*)			Orthorhombic (*Cmcm*)					Orthorhombic (*Pmma*)
Pressure (GPa)	0.0001	8.76	9.84	11.43		38	40	45	50		61
a (Å)	8.5469(3)	8.4309(8)	5.943(1)	5.930(1)		2.745(1)	2.741(1)	2.708(1)	2.685(1)		9.059(3)
b (Å)						9.393(2)	9.325(1)	9.238(2)	9.228(2)		2.658(1)
c (Å)			8.367(2)	8.284(2)		9.242(2)	9.223(2)	9.121(3)	9.099(3)		9.165(2)
Vol (Å³)	624.35	599.26	295.16	291.25		238.3(5)	235.7(2)	228.2(6)	225.4(9)		220.7(9)
	4-fold coordination		4-fold coordination								
Fe-O x 4	2.011(1)	1.9697(8)	1.964(4)	1.961(9)							
	6-fold coordination		6-fold coordination			6-fold coordination					6-fold coordination
(Fe,Ti)-O x 4	2.042(1)	2.018(1)	2.011(5)	1.995(2)	(Fe,Ti)-O2 x 1	1.936(4)	1.837(2)	1.808(3)	1.777(6)	Fe1-O22 x1	1.673(7)
- O x 2	2.042(1)	2.018(1)	2.021(2)	2.025(8)	-O2 x 2	1.704(2)	1.779(4)	1.729(4)	1.734(4)	-O32 x1	1.724(8)
Average	2.042(1)	2.018(1)	2.014(4)	2.005(4)	-O3 x 2	2.027(2)	1.931(3)	1.929(4)	1.924(6)	-O31 x2	1.825(7)
					-O1 x 1	2.348(3)	2.266(3)	2.338(3)	2.090(4)	-O12 x2	1.995(7)
					Average	1.958(3)	1.921(3)	1.911(4)	1.847(5)	Average	1.839(7)
										Ti-O11 x2	1.747(8)
										-O21 x1	1.754(8)
										-O31 x1	1.783(7)
										-O32 x2	2.082(8)
										Average	1.865(8)
					8-fold coordination					8-fold coordination
					Fe-O1 x 2	2.007(3)	2.111(2)	2.126(4)	2.375(5)	Fe2-O31 x4	2.187(6)
					-O2 x 4	2.324(3)	2.314(3)	2.323(3)	2.288(5)	-O22 x1	2.428(7)
					-O3 x 2	2.532(2)	2.521(2)	2.500(3)	2.468(5)	-O21 x2	2.454(7)
					Average	2.297(3)	2.315(3)	2.318(4)	2.355(5)	-O11 x1	2.553(8)
										Average	2.329(7)
										Fe3-O32 x4	2.285(7)
										-O22 x2	2.319(8)
										-O12 x2	2.445(8)
										Average	2.333(8)